Project 2020-366

Postdoctoral researcher: Pouria Bahrami Ataabadi – 9397156

Supervisor: Prof. Dr. Marcilio Alves

2025-2026

Report: Completed Activities During 2024–2025

P1. Improvement of the Friction Test Rig at the GMSIE Laboratory
Note: due to the client's lack of interest in supporting the original project (the friction characterization at higher velocities), this part of the project was replaced by two alternative studies (hygrothermal and thermal effect of the material degradation of CFRP laminated components, and effect of off-ceneter impact on the GFRP plates) and a material characterization campaign at higher strain rates for Marcopolo.

P2. Low-Velocity Impact (LVI) Testing on CFRP Composite Sandwich Panels
This activity included the development of a VUMAT material model for the simulation of LVI tests, as well as the execution of experimental LVI tests on CFRP sandwich panels.

Preparation of a paper from the study in 2022 (under review)

A Novel Multifunctional Solid-State Battery With Piezoelectric Response: Applications For Structural Health Monitoring

Denys Marques, Bruno G. Christoff, Pouria Ataabadi, João P. Carmo, Maria H. Braga, Marcílio Alves, and Volnei Tita

Abstract—The development of new solid-state batteries attends current demands for better energy storage devices and low environmental impact. The development of new and more efficient Structural Health Monitoring (SHM) systems can also have a positive impact on the sustainable use of resources by increasing safety and expanding the lifetime of components. Herein a new, multifunctional, solid-state battery with piezoelectric response is used as a sensor to monitor vibrations in an SHM system. The battery is attached to a composite beam which is subjected to a base acceleration condition. A tip mass is added to the free end of the beam to act as a pseudo-damage. The results showed that the new battery is capable of monitoring the dynamic excitation of the structure mainly for frequencies below 100 Hz. Despite the limitation to a low frequency range, the battery was used to successfully monitor two pseudo-damage scenarios, revealing excellent potential for future applications in SHM.

Index Terms— Multifunctional Battery, Solid-state Battery, Structural Health Monitoring, Vibration-based Method.

I. INTRODUCTION

D. Marques is with the Department of Mechanical Engineering, Federal Center of Technological Education Celso Suckow da Fonseca, , Angra dos Reis, RJ, Brazil (e-mail: denys.marques@cefet-rj.br).

B. G. Christoff is with the Institute of Lightweight Engineering and Polymer Technology, Dresden University of Technology, Dresden, Germany (e-mail: bruno.christoff@tu-dresden.de).

P. Ataabadi and M. Alves are with the Department of Mechatronics and Mechanical Systems Engineering, Engineering School of the University of São Paulo, University of São Paulo, São Paulo, SP, Brazil (e-mail: maralves@usp.br).

J. P. Carmo is with the Department of Electrical Engineering, São Carlos School of Engineering, University of São Paulo, São Carlos, SP, Brazil (e-mail: jcarmo@sc.usp.br).

M. H. Braga is with the Department of Engineering Physics, Faculty of Engineering of the University of Porto, Porto, Portugal and with the LAETA - INEGI, Institute of Science and Innovation in Mechanical and Industrial Engineering, Porto, Portugal (e-mail: mbraga@fe.up.pt).

V. Tita is with the Department of Aeronautical Engineering, São Carlos School of Engineering, University of São Paulo, São Carlos, SP, Brazil and with the Department of Mechanical Engineering, Fac-

THROUGHOUT its life, all structures or components are expected to degrade, be it by the steady action of a variable load (fatigue damage), by sudden events (such as impact and other accidental events), or even by flawed design. Regardless of the origin behind the presence (or increase) of damage in a component, the need for the development of safer machines and structures has pushed forward the research on Structural Health Monitoring (SHM) systems, which aims to provide continuous monitoring of the structural conditions. Among all SHM methods available, Vibration-based Methods (VBM) stand out due to their easy implementation and ability to monitor damage on a global scale [1]–[3]. They provide insights into the structural integrity and enable early detection of potential failures through subtle changes in vibration patterns [4].

Alongside the development of new strategies for SHM systems came the development of new sensing approaches for non-destructive testing. For instance, Ubertini et al [5] proposed two novel strain sensing technologies for dynamic monitoring of civil structures: one sensor is made of cementitious material and is specially designed for embedding applications in concrete, while the second is made of a flexible elastomer used for surface applications. The first sensor's principle of

Preparation of a paper from the material characterization in 2023-2025 (published)

Hot Isostatic Pressing Effects on Ductiles Fracture in Additive Manufactured Ti–6Al–4V Alloy: An Experimental and Numerical Approach

Original Research Article | Published: 19 March 2025

(2025) Cite this article

Mohammad Hossein Shaterzadeh ✉, Pouria B. Ataabadi, Larissa Driemeier & Marcilio Alves

Abstract

This study investigates the mechanical behavior of the Ti–6Al–4V alloy fabricated using electron beam melting through a hybrid experimental–numerical approach, focusing on ductile fracture under diverse loading conditions. A diverse specimen design is employed to evaluate fracture mechanisms in detail and to calibrate fracture models with high precision. The influence of porosity on mechanical behavior and fracture mechanisms is examined by comparing as-built specimens to those processed with hot isostatic pressing. Additionally, the effect of fabrication orientation relative to the build chamber on the mechanical properties of Ti–6Al–4V specimens is analyzed, offering insights into the behavior and optimization of additive manufacturing (AM) components. To predict fracture behavior, three numerical ductile fracture models—Johnson–Cook (JC), modified Mohr–Coulomb (MMC), and Hosford–Coulomb—are implemented using the VUMAT (User Material) subroutine. Based on these findings, a modified MMC model is proposed to address conditions involving both negative and positive triaxiality. The outcomes of this study provide a deeper understanding of the mechanical behavior of the Ti–6Al–4V alloy manufactured via AM, contributing to the improved design and optimization of AM components for industrial applications.

Preparation of a paper on the hygrothermal and thermal aging on the axial impact response of CFRP tubes in 2024-2025 (submitted)

Developing user-material subroutine for LVI simulation on CFRP sandwich panels and laminated composite panels

The scope of this study includes the following activities:

1. **Experimental Investigation of Low-Velocity Impact (LVI) on Laminated and Sandwich Panels**
   - Preparation and characterization of laminated composite panels made of S-glass/PEKK and CFRP/Nomex honeycomb sandwich panels.
   - Execution of low-velocity impact tests at various energy levels and impact locations (center and off-center) to assess the sensitivity of damage evolution and energy absorption mechanisms.
   - Post-impact evaluation through residual flexural strength tests (three-point bending) on impacted sandwich panels.

2. **Finite Element Modeling and Development of User-Material Subroutine**
   - Construction of detailed finite element models using Abaqus/Explicit to simulate LVI events on laminated and sandwich structures.
   - Implementation of a user-defined material subroutine (VUMAT) for the composite plies, incorporating intralaminar damage models based on stress-based failure criteria, element degradation, and deletion schemes.
   - Modeling of interlaminar failure using a surface-based cohesive zone model to capture delamination behavior under impact.

3. **Validation of Numerical Models**
   - Comparison of numerical predictions with experimental results in terms of force-displacement histories, absorbed energy, permanent indentation, damage area, and failure mechanisms.
   - Assessment of the performance and limitations of the developed numerical framework, particularly regarding the prediction of post-impact residual properties and damage morphology.

Brief description of VUMAT material sub for plain weave (PW) composites

A finite element (FE) model for simulating low-velocity impact on composite plates is developed using the Abaqus/Explicit commercial finite element software. The laminated composite plate is modeled by stacking multiple layers of continuum plies, allowing the simulation to capture both intralaminar and interlaminar responses during impact. This layered FE approach is designed to accurately predict the detailed mechanical behavior of composite plates under low-velocity impact conditions. The built-in surface-based cohesive model in Abaqus is employed to represent the inter-layer mechanical response.

Figure 1 illustrates the selected mechanical behavior of the composite ply. In the non-progressive damage response, the material exhibits elastic behavior (path AB) until the failure criterion is reached at point B. At this stage, the mechanical properties associated with the failure mode are instantaneously reduced to 90% of their initial values. Following this degradation, the failed element undergoes a near-complete unloading process (path BC) while remaining active in the simulation. This mechanical response is applied to composite plies in the in-plane directions (directions 1 and 2) as well as in the through-thickness direction (Z-direction) under both compressive and tensile stress conditions. To prevent excessive distortion of the failed element, an element deletion criterion is employed. Once this criterion is satisfied (point D), the failed element is removed from the simulation.

Fig. 1. Bilinear stress-strain response of inter-layer composite ply.

Intralamina response

A three-dimensional stress state user material subroutine (VUMAT) is employed to simulate the orthotropic behavior of composite plies. The stress-strain relationship for this 3D stress state is described by Eq. 1

$$\begin{bmatrix} \sigma_{11} \\ \sigma_{22} \\ \sigma_{33} \\ \sigma_{12} \\ \sigma_{23} \\ \sigma_{13} \end{bmatrix} = \begin{bmatrix} C_{11} & C_{12} & C_{13} & & & \\ & C_{22} & C_{23} & & Zeros & \\ & & C_{33} & & & \\ & & & 2C_{44} & & \\ & Sym & & & 2C_{55} & \\ & & & & & 2C_{66} \end{bmatrix} \begin{bmatrix} \varepsilon_{11} \\ \varepsilon_{22} \\ \varepsilon_{33} \\ \varepsilon_{12} \\ \varepsilon_{23} \\ \varepsilon_{13} \end{bmatrix} \qquad (1)$$

By introducing appropriate damage variables, that degrade the components of the stiffness matrix Eq.1 will represent the material's response under both intact (undamaged) and damaged conditions regarding the value of the corresponding damage variables. Consequently, the general form of the stiffness matrix components is presented in Eq. 2.

$$C_{11} = (1 - d_f)C_{11}^0 \qquad \text{(a)}$$

$$C_{22} = (1 - d_f)C_{22}^0 \qquad \text{(b)}$$

$$C_{33} = (1 - d_m)C_{33}^0 \qquad \text{(c)}$$

$$C_{12} = (1 - d_f)(1 - d_m)C_{12}^0 \qquad \text{(d)}$$

$$C_{23} = (1 - d_f)(1 - d_m)C_{23}^0 \qquad \text{(e)}$$

$$C_{13} = (1 - d_f)(1 - d_m)C_{13}^0 \qquad \text{(f)}$$

$$G_{12} = (1 - d_f)(1 - d_{mc})C_{44}^0 \quad , C_{44}^0 = G_{12} \qquad \text{(g)}$$

$$G_{23} = (1 - d_f)(1 - d_{mt})(1 - d_{mc})C_{23}^0 \quad , C_{55}^0 = G_{23} \qquad \text{(h)}$$

$$G_{13} = (1 - d_f)(1 - d_{mt})(1 - d_{mc})C_{13}^0 \quad , C_{66}^0 = G_{13} \qquad \text{(i)}$$

(2)

There are two types of damage variables in Eq. 2; (I) fiber dominant damage variables (d_f) and (II) matrix dominant damage variables (d_m). In this study, the same amount of fibers are placed in two in-plane orthogonal directions of composite (1-direction and 2-direction), thus, d_{f1} and d_{f2} are fiber damage variables due to fiber failure modes in 1-direction and 2-direction, respectively. Besides fiber dominant failure modes, the composite plies can fail due to matrix damage failure modes where matrix damage variable d_m degrades the corresponding components of stiffness matrix as expressed in Eq.2. All damage variables are defined in Eq. 3.

$$d_{f1} = 1 - (1 - d_{f1t})(1 - d_{f1c}) \qquad \text{(a)}$$

$$d_{f2} = 1 - (1 - d_{f2t})(1 - d_{f2c}) \qquad \text{(b)}$$

(3)

$$d_f = 1 - (1 - d_{f1})(1 - d_{f2}) \tag{c}$$

$$d_m = 1 - (1 - d_{mt})(1 - d_{mc}) \tag{d}$$

Note: The subscripts c and t denote compression and tension failure modes, respectively.

The initial (undamaged) components of the stiffness matrix, C_{ij}^0, in Eq. 2 are calculated using the formulas provided in Eq.4.

$$C_{11}^0 = E_{11}(1 - v_{23}v_{32})\Delta \tag{a}$$

$$C_{22}^0 = E_{22}(1 - v_{13}v_{31})\Delta \tag{b}$$

$$C_{33}^0 = E_{33}(1 - v_{12}v_{21})\Delta \tag{c}$$

$$C_{12}^0 = E_{11}(v_{21} - v_{31}v_{23})\Delta \tag{d}$$

$$C_{13}^0 = E_{11}(v_{31} - v_{21}v_{32})\Delta \tag{e}$$

$$C_{23}^0 = E_{22}(v_{32} - v_{12}v_{31})\Delta \tag{f}$$

$$\Delta = \frac{1}{(1 - v_{21}v_{12} - v_{32}v_{23} - v_{13}v_{31} - 2v_{13}v_{21}v_{32})}$$

(4)

The material model incorporates six independent damage variables (d_{mt}, d_{mc}, d_{f1t}, d_{f1c}, d_{f2t}, d_{f2c}) under compressive and tensile loading conditions. All fiber and matrix dominant damage variables can take one of two values: (I) zero, representing the undamaged condition, and (II) a maximum value (d_{max} =0.90) when the damage criterion is met when a damage variable turns equal to 0.90 it will remain constant during the simulation. In other words, the material exhibits linear elastic behavior until a failure criterion is satisfied, at which point the corresponding damage variable instantaneously reaches its maximum value. Consequently, the associated components of the stiffness matrix are degraded by Eq. 2.

Six failure criteria are employed to account for intralaminar damage. As previously mentioned, for plain weave composite plies under investigation, an equal amount of fibers is present in both the 1- and 2-directions. Therefore, unlike unidirectional plies, fiber damage (due to compression and tension) is considered in both the 1- and 2-directions. Matrix failure modes

under compression and tension are also taken into account to characterize damage in the out-of-plane (Z-direction). All failure modes are detailed in Eq. 5.

Fiber failure tension in i-direction (i=1,2)	$f_{ft}^i = \left(\dfrac{\sigma_i}{X_i^T}\right) + \left(\dfrac{\tau_{12}}{S_{12}}\right) + \left(\dfrac{\tau_{i3}}{S_{i3}}\right) \geq 1$	(a)
Fiber failure compression in i-direction (i=1,2)	$f_{fc}^i = \left(\dfrac{\sigma_i}{X_i^C}\right) + \left(\dfrac{\tau_{12}}{S_{12}}\right) + \left(\dfrac{\tau_{i3}}{S_{i3}}\right) \geq 1$	(b)
Matrix failure tension out-of-plane direction	$f_{mt} = \left(\dfrac{\sigma_3}{Y_Z^T}\right) + \left(\dfrac{\tau_{13}}{S_{13}}\right) + \left(\dfrac{\tau_{23}}{S_{23}}\right) \geq 1$	(c)
Matrix failure compression out-of-plane direction	$f_{mc} = \left(\dfrac{\sigma_3}{Y_Z^C}\right) + \left(\dfrac{\tau_{13}}{S_{13}}\right) + \left(\dfrac{\tau_{23}}{S_{23}}\right) \geq 1$	(d)

(5)

To prevent excessive distortion of failed elements, an element deletion criterion is implemented in the VUMAT code. The decision to remove an element from the simulation is based on the ratio of the element's cu

rrent volume to its initial volume. Through a process of trial and error, the upper and lower thresholds for this ratio were determined to be 1.85 and 0.55, respectively.

To validate and enhance the material model, two studies were considered. The first study, Experimental and Numerical Analysis of Laminated Composite Panels Subjected to Low-Velocity Impact at Different Locations, is a collaborative experimental–numerical investigation conducted with international researchers. The second study, Impact on CFRP Sandwich Panels with Nomex Honeycomb Core, was entirely carried out at the GMSIE laboratory.

Experimental and Numerical analysis of Laminates Composite Panel Subjected to Low-velocity Impact at Different Locations

1. Introduction

Due to their unique properties such as light weight and strength/stiffness to weight ratio, fibre reinforced plastics (FRPs) are now becoming more widely employed in the aerospace, defence, and automotive industries as an alternative to conventional metallic materials such as aluminium and steel. FRPs fabricated by stacking unidirectional prepregs are used mainly in the aircraft sectors, but these composites exhibit relatively a low damage tolerance under transverse impact loading conditions. During service, composite structures can be exposed to impact loadings by foreign bodies such as dropped tools during maintenance, bird-strike, runway debris (FOD), and hailstones etc. The damage resulting from this type of loading is particularly difficult to detect and assess as it is often invisible to the naked eye. However, this type of damagecan lead to a catastrophic failure of a composite structure [1]–[3]. Therefore, considerable research work aimed at understanding the impact response of these materials can be found in the literature [4]–[10]. For example, an early review of continuous fibre reinforced composites subjected to impact loadings is presented by Cantwell and Morton[4]. The response of carbon fibres (CFs) and glass fibres (GFs) reinforced epoxy panels subjected to central repeated low velocity impacts has been investigated in-depth both experimentally and numerically by several researchers [11]–[18].

From the current body of research, it can be seen that the focus is on the investigation of the impact response of fibre reinforced laminates under single or multiple impacts at a nominal centre location, i.e., at a location geometrically symmetrical to the support boundaries. However, during service, impacts scenarios must be expected and evaluated at various locations on a structure. This is especially serious for the case of damage resulting from an impact near a structural boundary or discontinuity, such as a support or joint, where it may weaken the overall integrity of the composite structure [19]. The behaviour of a GFs/Epoxy laminate impacted near an edge and on an edge was investigated experimentally and numerically using ABAQUS software by Malhotra et al., [20]. Their results showed that a higher impact energy leads to more energy being absorbed by the panels at both these impact positions. It was also shown that the delamination between plies and fibre breakage were more sever at on edge impact location. Reis et al., [21] investigated the response of repaired epoxy-based laminates under repeated impacts at different locations. The

authors concluded that the impact behaviour of composite structure can be determined by the stress concentration generated by a boundary condition. The behavior of CFs/Epoxy laminates subjected to double impact locations with same distance (i.e. four impact distances) from the centre was compared by Liao et al., [22]. These results showed that, as the impact position becomes closer to a boundary condition, the incident energy is dissipated mainly by the delamination between the plies.

This review of the literature shows that, due to their strength, durability and relatively low cost, numerous works have been conducted on the behaviour of high-performance epoxies-based composites laminates subject to impact loading. However, these composites suffer some serious limitations such as brittleness, low damage tolerance, poor recyclability, and their propensity to generate toxic fumes due to their low combustibility. Therefore, research in this area has seen a move toward replacing epoxies by thermoplastic resins which have better toughness, good impact properties, shorter manufacturing time, better recyclability and less sophisticated equipment to store thermoplastic pre-impregnated materials [23]. Jang et al., [24] compare the response of thermoplastic and thermoset laminates under central multiple impact loadings. These authors highlighted the superiordamage tolerance of thermoplastic composites when compared to the corresponding epoxy-based laminates. The traditional thermoplastic resins such as polypropylene (PP), polyethylene (PE) and nylon reinforced (using different types of fibres) were the most commonly used composites [25]. However, the utilisation of these thermoplastics is limited due to their low thermal resistance at high temperature, low moduli, low glass transition temperature (Tg) and relatively low chemical resistance [26].

The issues of using traditional thermoplastic in aerospace industry are solved by using high performance thermoplastic polymers such as poly-ether-ketone-ketone (PEKK). High-performance fibres reinforced PEKK polymers have demonstrated an exceptional impact resistance and high thermal stability at high temperatures [27]. In the open literature, the data of PEKK based-composites are limited and more investigations are necessary to deepen the understanding about the behaviour of these newly developed composites under various loading conditions. The compression strength and interlaminar shear strength [28], flexural strength [29], elasto-plastic behaviour [30] and thermal degradation [31] of CFs/PEKK composites have been investigated. Their highstrength and stiffness compared to GFs is one of the reasons why the

somewhat limited number of investigations have focused on using CFs as reinforcing materials with PEKK.

Regarding fibre-metal laminates (FMLs), the high cost and the galvanic corrosion problems with aluminium alloys are major issues relating to their used in aerospace industry[32]. S-glass (S-GF), as a high-strength filler is a good candidate to replace CFs for the manufacture of FMLs. Nassir et al., [23], [33], [34] investigated experimentally and numerically the perforation response of S-GFs reinforced PEKK either as plain composite or within an FML construction. These authors highlighted the superiority of these newly developed composites over the corresponding GFs/Epoxy laminates.

It is interesting to note that there is no work in the open literature focused on investigating the impact response of such kind of high-performance composites at different locations relative to a boundary. Therefore, the aim of this investigation is to evaluate the response of woven S-GFs reinforced PEKK panels subjected to central and off-centre impact positions. To facilitate this, laminate panel specimens were manufactured and subjected to a series of transverse impact loadings at various positions using a drop weigh impact testing machine. The results from this experimental work were compared to those from a finite element analysis (FEA) model that was developed to predict the response of such a material subjected to the same impact loading scenarios.

2. Materials and experimental procedure

Initially, the thermoplastic prepregs investigated in this work were based on woven S-glass fibres (124 gms) supplied by East Coast fibreglass, UK, and PEKK (KEPSTAN-6003 PL) supplied by ARKEMA, France. The PEKK is provided in a powdered form with particle size of 50 microns. A powder impregnation technique was used to prepare the pre-impregnated fibre plies (prepregs) as described in more detail by Nassir et al., [23]. Eight prepregs plies were stacked in a square mould with inner dimensions of 100 mm x 100 mm and subjected to a compression force and heating cycle, using a hot press, to consolidate the stack. The cycle comprised heating the stack to 330 ºC at a rate of 5 ºC/min and holding this temperature for 30 minutes while maintaining a pressure of 3 bar before cooling to room temperature inside the hot press at a rate of 2 ºC/minute. The finished panels were then removed and extracted from the mould.

The resulting panels were then inspected before subjecting them to a series of low velocity impact loadings using a guided drop weight apparatus shown schematically in

Figure 1a. The panel laminate specimens were clamped rigidly on all four sides using a rigid clamp frame secured with eight fastening bolts as shown in Figure 1 and 2. The bolts were tightened with the same torque to ensure uniform fixing at the clamped boundary. The impact energy was adjusting by altering the initial drop hight of the impactor which was guided to the selected impact location by two vertical guide rails. The impactor comprised a 0.7 kg mass fitted with a hemispherical indenter of diameter of 12.5 mm that included a piezo-electric load-cell located between the indenter and the impactor mass. A data acquisition system was used to measure and record the contact force vs. time history for each impact test. At the same time, the indentor displacement against time was measured using a high-speed camera (HSC) type (MotionPro-X4) placed in front of the specimen to track the movement of the impactor. In the post-test analysis, the Proanalysis software package was used to process the motion of the indentor in order to provide a cross-check for the final displacement vs. time result. After impacting a laminate panel specimen, the impactor was caught manually after the first rebound to avoid any repeated impacts.

The laminate panel specimens were impacted at centre and off-centre locations shown in Figure 2 using energies 1 Joule, 2 Joules J, 3 Joules and 4 Joules impact energies that were achieved by adjusting the hight of the impactor accordingly. The four impact locations used in this investigation are shown in **Error! Reference source not found.**.
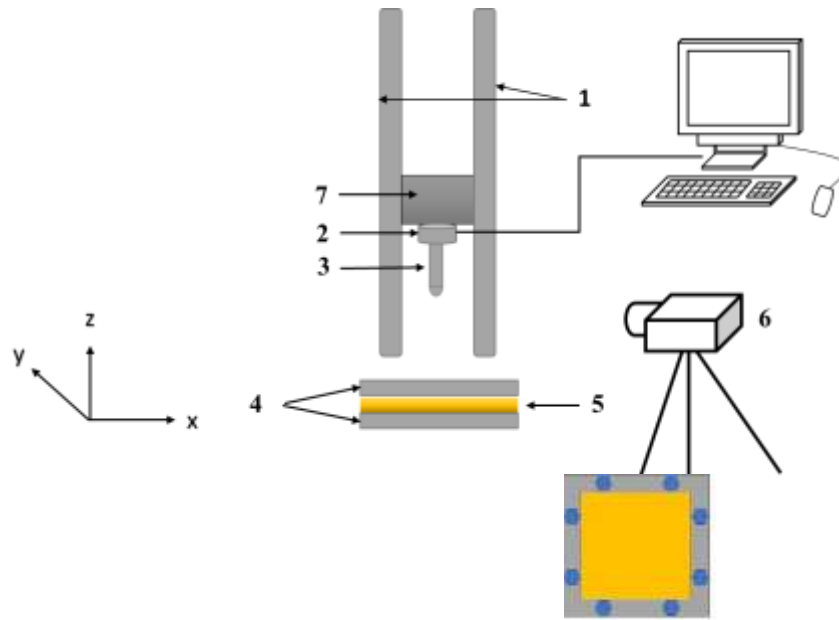
Figure 1a. The setup of low velocity impact tests, (1) guided rules, (2) load cell, (3) indentor, (4) test fixture, (5) laminate panel specimen, (6) HSC, (7) drop mass.
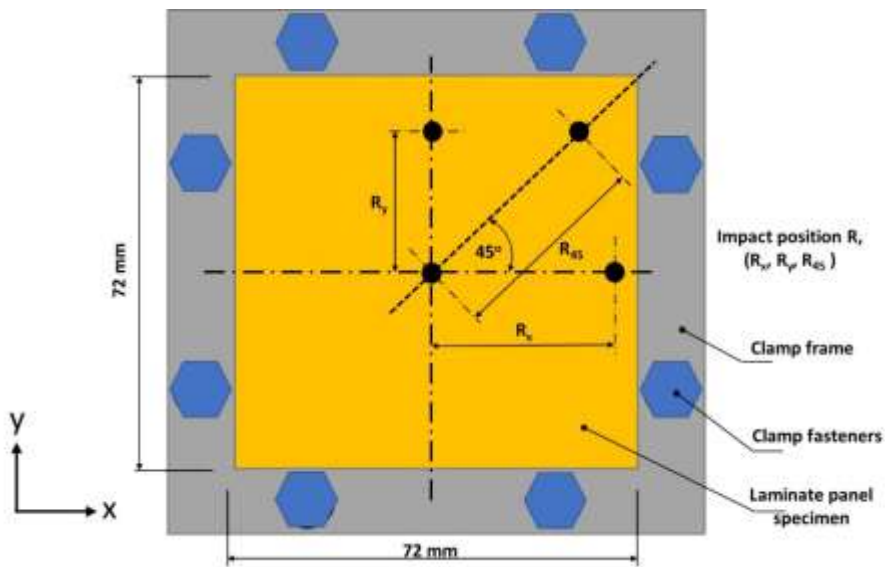
Figure 2 . Positions of the impact test points.

3. Finite element modelling

. Finite element model

A finite element (FE) model for simulating low-velocity impact on composite plates is developed using the Abaqus/Explicit commercial finite element software. The laminated composite plate is modeled by stacking multiple layers of continuum plies, allowing the simulation to capture both intralaminar and interlaminar responses during impact. This layered FE approach is designed to accurately predict the detailed mechanical behavior of composite plates under low-velocity impact conditions. The built-in surface-based cohesive model in Abaqus is employed to represent the inter-layer mechanical response.

Figure 1 illustrates the selected mechanical behavior of the composite ply. In the non-progressive damage response, the material exhibits elastic behavior (path AB) until the failure criterion is reached at point B. At this stage, the mechanical properties associated with the failure mode are instantaneously reduced to 90% of their initial values. Following this degradation, the failed element undergoes a near-complete unloading process (path BC) while remaining active in the simulation. This mechanical response is applied to composite plies in the in-plane directions (directions 1 and 2) as well as in the through-thickness direction (Z-direction) under both compressive and tensile stress conditions. To prevent excessive distortion of the failed element, an element deletion criterion is employed. Once this criterion is satisfied (point D), the failed element is removed from the simulation.

Fig. 1. Bilinear stress-strain response of inter-layer composite ply.

Intralamina response

A three-dimensional stress state user material subroutine (VUMAT) is employed to simulate the orthotropic behavior of composite plies. The stress-strain relationship for this 3D stress state is described by Eq. 1

$$
\begin{bmatrix} \sigma_{11} \\ \sigma_{22} \\ \sigma_{33} \\ \sigma_{12} \\ \sigma_{23} \\ \sigma_{13} \end{bmatrix} = \begin{bmatrix} C_{11} & C_{12} & C_{13} & & Zeros & \\ & C_{22} & C_{23} & & & \\ & & C_{33} & & & \\ & & & 2C_{44} & & \\ & Sym & & & 2C_{55} & \\ & & & & & 2C_{66} \end{bmatrix} \begin{bmatrix} \varepsilon_{11} \\ \varepsilon_{22} \\ \varepsilon_{33} \\ \varepsilon_{12} \\ \varepsilon_{23} \\ \varepsilon_{13} \end{bmatrix} \tag{1}
$$

By introducing appropriate damage variables, that degrade the components of the stiffness matrix Eq.1 will represent the material's response under both intact (undamaged) and damaged conditions regarding the value of the corresponding damage variables. Consequently, the general form of the stiffness matrix components is presented in Eq. 2.

$$C_{11} = (1 - d_f)C_{11}^0 \tag{a}$$

$$C_{22} = (1 - d_f)C_{22}^0 \tag{b}$$

$$C_{33} = (1 - d_m)C_{33}^0 \tag{c}$$

$$C_{12} = (1 - d_f)(1 - d_m)C_{12}^0 \tag{d}$$

$$C_{23} = (1 - d_f)(1 - d_m)C_{23}^0 \tag{e}$$

$$C_{13} = (1 - d_f)(1 - d_m)C_{13}^0 \tag{f}$$ (2)

$$G_{12} = (1 - d_f)(1 - d_{mc})C_{44}^0 \quad , C_{44}^0 = G_{12} \tag{g}$$

$$G_{23} = (1 - d_f)(1 - d_{mt})(1 - d_{mc})C_{23}^0 \quad , C_{55}^0 = G_{23} \tag{h}$$

$$G_{13} = (1 - d_f)(1 - d_{mt})(1 - d_{mc})C_{13}^0 \quad , C_{66}^0 = G_{13} \tag{i}$$

There are two types of damage variables in Eq. 2; (I) fiber dominant damage variables (d_f) and (II) matrix dominant damage variables (d_m). In this study, the same amount of fibers are placed in two in-plane orthogonal directions of GFRP composite (1-direction and 2-direction), thus, d_{f1} and d_{f2}

are fiber damage variables due to fiber failure modes in 1-direction and 2-direction, respectively. Besides fiber dominant failure modes, the composite plies can fail due to matrix damage failure modes where matrix damage variable d_m degrades the corresponding components of stiffness matrix as expressed in Eq.2. All damage variables are defined in Eq. 3.

$$d_{f1} = 1 - (1 - d_{f1t})(1 - d_{f1c}) \tag{a}$$
$$d_{f2} = 1 - (1 - d_{f2t})(1 - d_{f2c}) \tag{b}$$
$$d_f = 1 - (1 - d_{f1})(1 - d_{f2}) \tag{c}$$
$$d_m = 1 - (1 - d_{mt})(1 - d_{mc}) \tag{d}$$

(3)

Note: The subscripts c and t denote compression and tension failure modes, respectively.

The initial (undamaged) components of the stiffness matrix, C_{ij}^0, in Eq. 2 are calculated using the formulas provided in Eq.4.

$$C_{11}^0 = E_{11}(1 - v_{23}v_{32})\Delta \tag{a}$$
$$C_{22}^0 = E_{22}(1 - v_{13}v_{31})\Delta \tag{b}$$
$$C_{33}^0 = E_{33}(1 - v_{12}v_{21})\Delta \tag{c}$$
$$C_{12}^0 = E_{11}(v_{21} - v_{31}v_{23})\Delta \tag{d}$$
$$C_{13}^0 = E_{11}(v_{31} - v_{21}v_{32})\Delta \tag{e}$$
$$C_{23}^0 = E_{22}(v_{32} - v_{12}v_{31})\Delta \tag{f}$$

(4)

$$\Delta = \frac{1}{(1 - v_{21}v_{12} - v_{32}v_{23} - v_{13}v_{31} - 2v_{13}v_{21}v_{32})}$$

The material model incorporates six independent damage variables (d_{mt}, d_{mc}, d_{f1t}, d_{f1c}, d_{f2t}, d_{f2c}) under compressive and tensile loading conditions. All fiber and matrix dominant damage variables can take one of two values: (I) zero, representing the undamaged condition, and (II) a maximum value (d_{max} =0.90) when the damage criterion is met when a damage variable turns equal to 0.90 it will remain constant during the simulation. In other words, the material exhibits linear elastic behavior until a failure criterion is satisfied, at which point the corresponding damage variable

instantaneously reaches its maximum value. Consequently, the associated components of the stiffness matrix are degraded by Eq. 2.

Six failure criteria are employed to account for intralaminar damage. As previously mentioned, for plain weave GFRP composite plies under investigation, an equal amount of fibers is present in both the 1- and 2-directions. Therefore, unlike unidirectional plies, fiber damage (due to compression and tension) is considered in both the 1- and 2-directions. Matrix failure modes under compression and tension are also taken into account to characterize damage in the out-of-plane (Z-direction). All failure modes are detailed in Eq. 5.

Fiber failure tension in i-direction $(i=1,2)$	$f_{ft}^i = \left(\dfrac{\sigma_i}{X_i^T}\right) + \left(\dfrac{\tau_{12}}{S_{12}}\right) + \left(\dfrac{\tau_{i3}}{S_{i3}}\right) \geq 1$	(a)
Fiber failure compression in i-direction $(i=1,2)$	$f_{fc}^i = \left(\dfrac{\sigma_i}{X_i^C}\right) + \left(\dfrac{\tau_{12}}{S_{12}}\right) + \left(\dfrac{\tau_{i3}}{S_{i3}}\right) \geq 1$	(b)
Matrix failure tension out-of-plane direction	$f_{mt} = \left(\dfrac{\sigma_3}{Y_Z^T}\right) + \left(\dfrac{\tau_{13}}{S_{13}}\right) + \left(\dfrac{\tau_{23}}{S_{23}}\right) \geq 1$	(c)
Matrix failure compression out-of-plane direction	$f_{mc} = \left(\dfrac{\sigma_3}{Y_Z^C}\right) + \left(\dfrac{\tau_{13}}{S_{13}}\right) + \left(\dfrac{\tau_{23}}{S_{23}}\right) \geq 1$	(d)

(5)

To prevent excessive distortion of failed elements, an element deletion criterion is implemented in the VUMAT code. The decision to remove an element from the simulation is based on the ratio of the element's current volume to its initial volume. Through a process of trial and error, the upper and lower thresholds for this ratio were determined to be 1.85 and 0.55, respectively.

Interlaminar response

A surface-based cohesive model with a traction-separation law is employed between adjacent composite plies to simulate the interlaminar cohesive response in the laminated plate. This approach is commonly used in numerical simulations of composite structures. For conciseness, only the key features of the interface model are summarized in Table 1.

Table 1. Cohesive surface features.

Traction-separation law	$\begin{Bmatrix} t_n \\ t_s \\ t_t \end{Bmatrix} = \begin{bmatrix} E_{nn} & 0 & 0 \\ & E_{ss} & 0 \\ Sym & & E_{tt} \end{bmatrix} \begin{Bmatrix} \varepsilon_n \\ \varepsilon_s \\ \varepsilon_t \end{Bmatrix}$
Damage initiation criterion	$max\left\{ \dfrac{\langle t_n \rangle}{t_n^0}, \dfrac{t_s}{t_s^0}, \dfrac{t_t}{t_t^0} \right\} = 1$
Damage evolution	$d = \dfrac{\delta_m^f (\delta_m - \delta_m^0)}{\delta_m (\delta_m^f - \delta_m^0)}$
Mixed mode propagation criterion	$G^C = G_n^C + (G_s^C - G_n^C)\left\{ \dfrac{G_s}{G_T} \right\}^{\eta}$

Interface mechanical properties are listed in Table 2.

Table 2. Interface mechanical properties.

t_n^0 (MPa)	$t_s^0 = t_t^0$ (MPa)	G_n^C ($\frac{N}{mm^2}$)	G_s^C ($\frac{N}{mm^2}$)	η
55	72	0.329	2.215	1.45

.

Table 2. Mechanical properties of plain weave S-glass fabric.

Elastic moduli	E_1	26 GPa	Shear moduli	G_{12}	2.6 GPa
	E_2			G_{13}	
	E_3	26 GPa		G_{23}	
Poisson's ratio	ν_{12}	0.15			
	ν_{13}				
	ν_{23}				
Strength parameters					
Tensile strength fiber direction	X_i^T	304 (MPa)	i ∈ 1-direction and 2-direction		
Compressive strength fiber direction	X_i^C	200 (MPa)	i ∈ 1-direction and 2-direction		
Tensile strength fiber direction	Y_z^T	169 (MPa)			

Compressive strength fiber direction	Y_z^C	111 (MPa)
Shear strength in all directions	S	50.4 (MPa)

(a)   ,   (b)

(c)   (d)
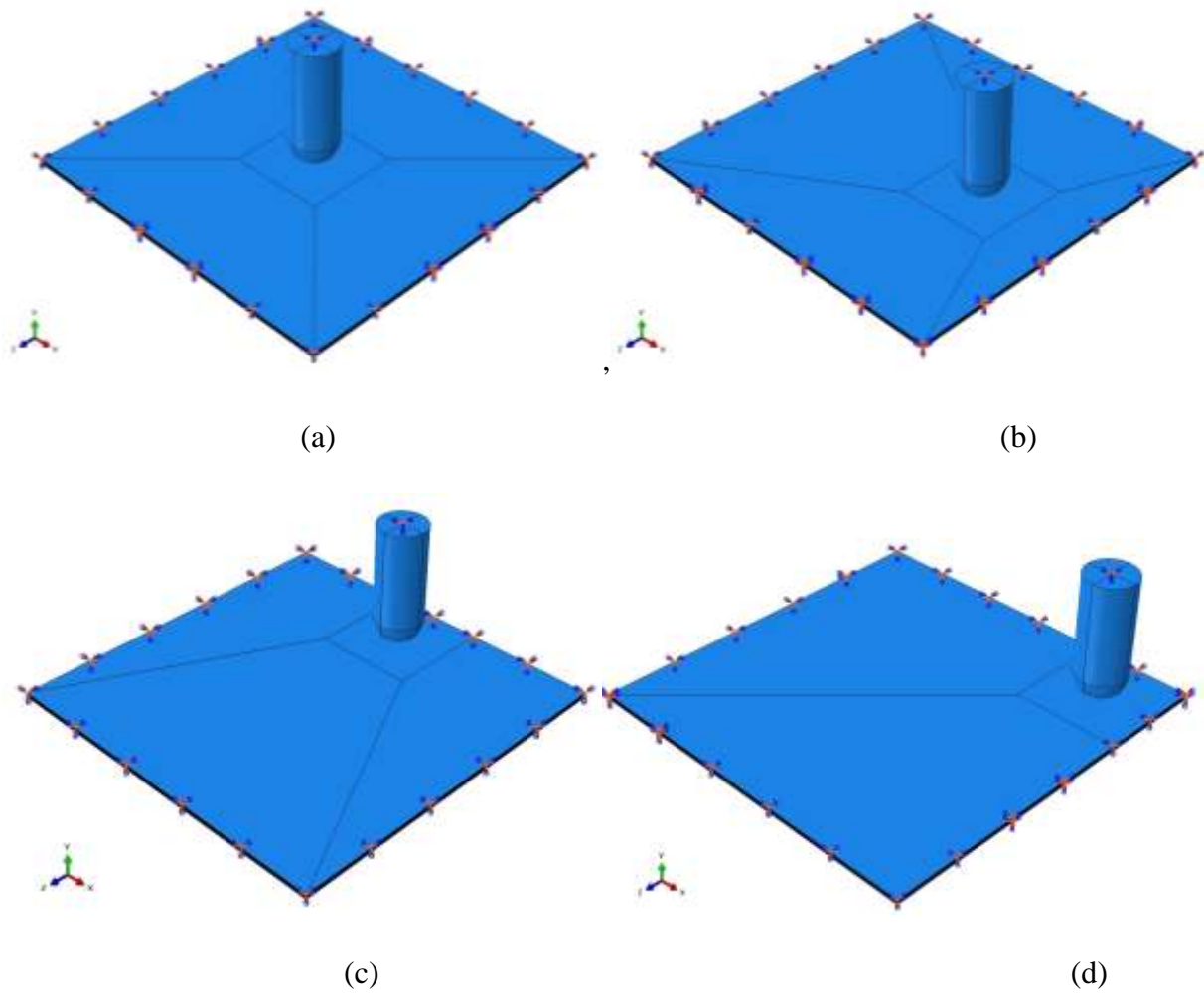
Figure 2. Geometry and boundary condition of the FEA model for GF/PEKK laminates subjected to low velocity impact at various impact locations.

4. Results and Discussion

4.1 Experimental testing

For each impact test, a vertical displacement vs. time history of the drop mass was derived from the double integration of the force vs. time data and considering Newton's second law,

$$P = m(a + g) \qquad (2)$$

where a is the acceleration of the drop-mass

These force vs. time and derived displacement vs. time curves were correlated to establish the force vs. displacement relationships shown in Figure 3 a-d which provided further insight into the impact response of the laminate panels. It can be seen that all curves exhibit a similar trend where the force increases to the maximum value before falling off to zero and with some residual (permanent) displacement. It is interesting to note Figures 4c and 4d, that panels impacted at the higher energies of 3 Joules and 4 Joules, respectively, exhibit a sharp drop in the contact force after reaching a maximum value. This behaviour is indicative of fibre breakage associated with the delamination failure mode as being the means of absorbing the energy of the impact.

It can also be observed from Figure 4 that a similar trend is exhibited at all impact energies where the ascending slope of the force vs. displacement recording increases when the impact position is moved from central toward the clamped boundary. This is due to the variation bending stiffness in the laminate specimen which increases at positions nearer to the clamped boundary condition. It can also be seen that, for the range of impact energies investigated here, the residual displacement after each impact decreases at positions away from the centre.

(a)   (b)

(c)   (d)
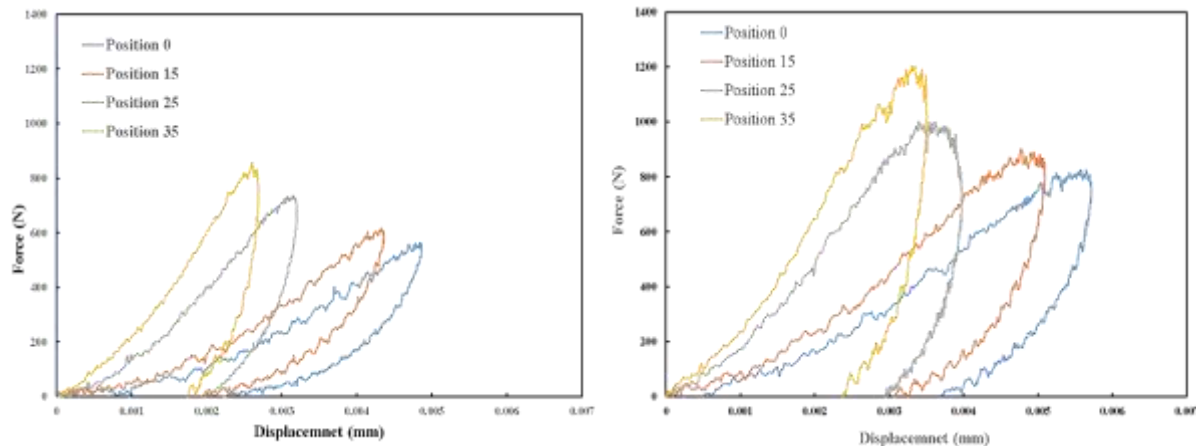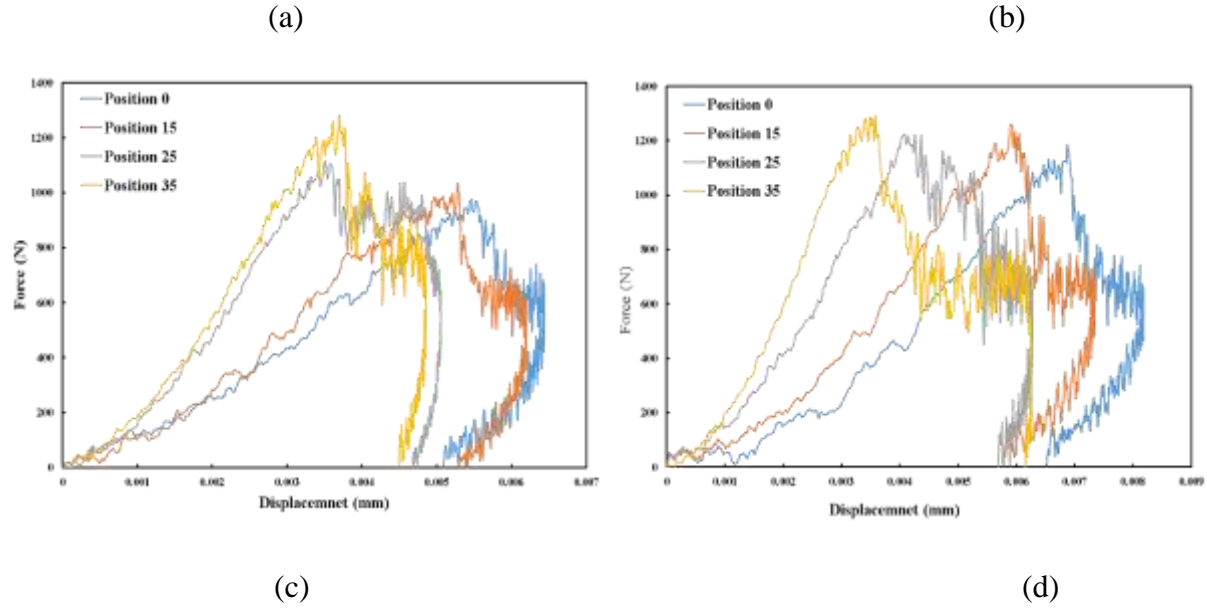
Figure 3. Force versus displacement for the 8-ply GF/PEKK laminates subjected to low velocity impact at various impact locations, (a) 1J, (b) 2J, (c) 3J and (d) 4J, respectively.

Bending stiffness values were obtained from the gradient of load vs. displacement recordings in Figure 4 and are listed in Table 1 together with different energies and impact locations. It can be observed from this table that, for the range of energies used, that the apparent bending stiffness increases with the impact energy. The results are not surprising Due to nature of the impact loading at which the inertia and the rate sensitivity of the tested panels play a role in increasing the values of the values of bending stiffness. It is worth mentioning that the 35 mm of centre exhibits the highest values of bending stiffness. This location is a special scenario as the impact position is close to two orthogonal boundaries comparing to one boundary for other positions.

Table 1. Bending stiffness values for the laminate investigated.

Position R [mm]	Impact energy [J]			
	1	2	3	4
0	150	196	213	243
$R_x = 15$	200	244	263	300

| $R_y = 25$ | 300 | 340 | 420 | 440 |
| $R_{45} = 35$ | 390 | 435 | 500 | 533 |

Clearly, Figure 3 shows the influence of impact energy and impact position on the resulting peak force, maximum displacement and residual displacement. The variation of the peak force and maximum displacement values with respect to impact position for the laminates studied subjected to various impact energies are shown in Figure 4a and Figure 4b, respectively. An inspection of the Figure 4a indicates that the values of maximum forces increase with the impact energy for all impact positions investigated. For example, at central impact (position 0), when the impact energy increases from 1J to 4 J, a significant increasing in the peak forces from 564 N to 1184 N was observed. It can also be seen that as the distance of an impact from centre increases, the increasing rate of peak forces decreases, highlighting the reduction in the bending stiffness near the boundary condition. The data of Figure 4a was fitted linearly to generate equations can be used to predict the evolution of peak forces with the impact positions. It is worth noting that the R^2 values of the linear trend fitting decrease with impact energy due to the higher damage introduced at higher energies. Figure 4b shows the relationship between the maximum displacement and off-centre impact positions for different impact energies. As expected, the values of maximum displacement enhance with the increase of impact energy as the higher impact energies cause shear failure and sever damage to the panels. However, at all impact energies, the maximum displacement values decrease linearly with the distance from centre, due to the bending stiffness reduction. This analysis suggesting that damage resistance of laminates shows a high dependency on the bending stiffness.
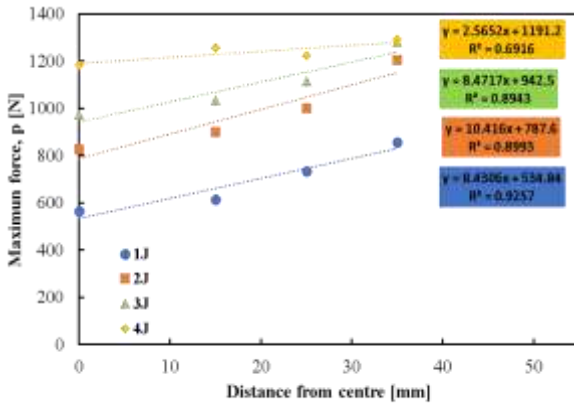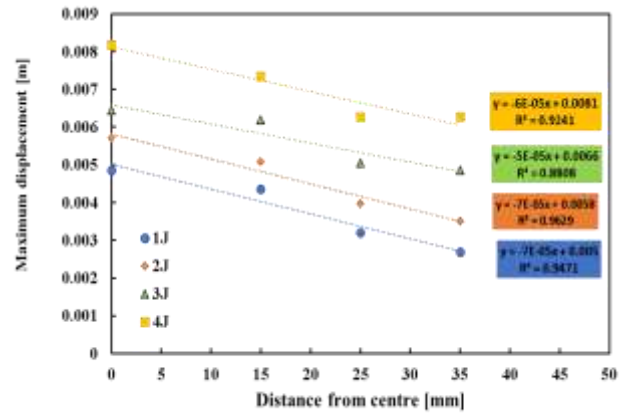
(a)   (b)
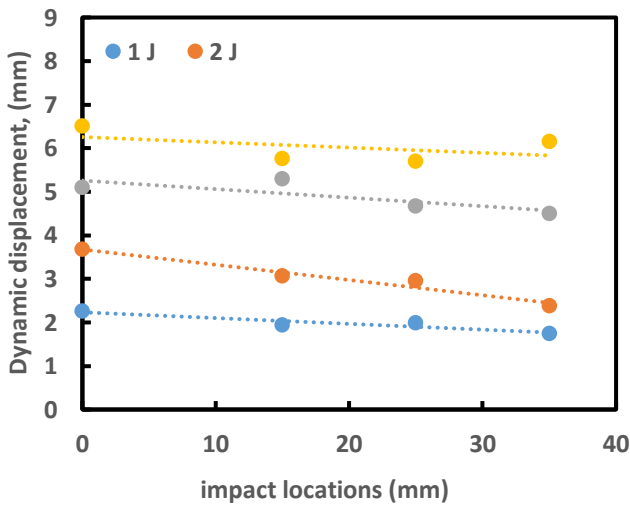
Figure 4. Maximum displacement (a) and maximum displacement (b) against impact position for GF/PEKK impacted at various energies.
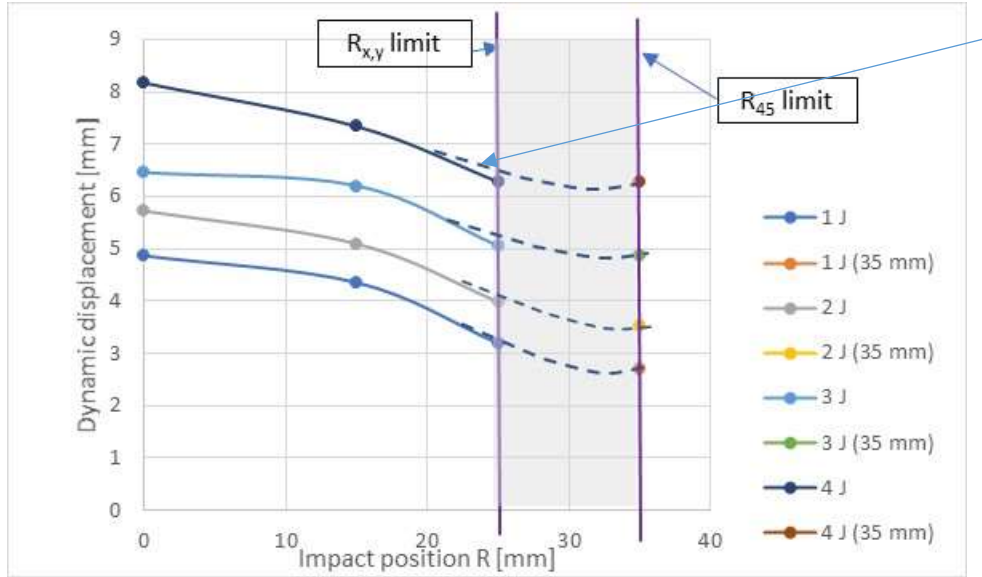
The energy absorbed by the specimens during impact process was evaluated considering the areas under the load vs. displacement curves in Figure 4. This was cross-correlated to provide the energy vs. time curves for all impact energies and locations as shown in Figure 5 a-d. It can be seen that these curves indicate an energy transfer profile that follows three stages: 1), initial contact between the indentor surface and panel target, 2) the initial kinetic energy of the indenter is transferred to the laminate panel (i.e., at the point where zero indenter velocity occurs), and 3) some energy is transferred back to the indenter as a rebound (upwards) with the rest being absorbed permanently through the actions of material failure and friction.

Regarding the impact positions, it is seen that the contact time required to reach the point where zero indenter velocity occurs (i.e., maximum energy transfer) reduces as the impact position move away from the center for the first three impact energies. However, panels impacted at higher energy (4 J) show no obvious differences in this contact time, indicating the severity if this energy level at all impact positions investigated. In the second stage any stored strain energy (elastic) in the panel is released back to the indenter accelerating it upwards until a maximum rebound velocity occurs. From this, an energy balance can be determined and equated to the amount of permanent damage occurring in the laminate material. Clearly, from Figure 6, impact positions closer to the boundary condition absorb less energy For the small impact energies (1 J and 2 J) the tree stages

can be distinguished easily, suggesting delamination is the main failure mode. However, panels impacted at 3J and 4 J exhibited less recoverable strain energy, highlighting the severity of these energy levels.

(a)

(b)

(c)

(d)
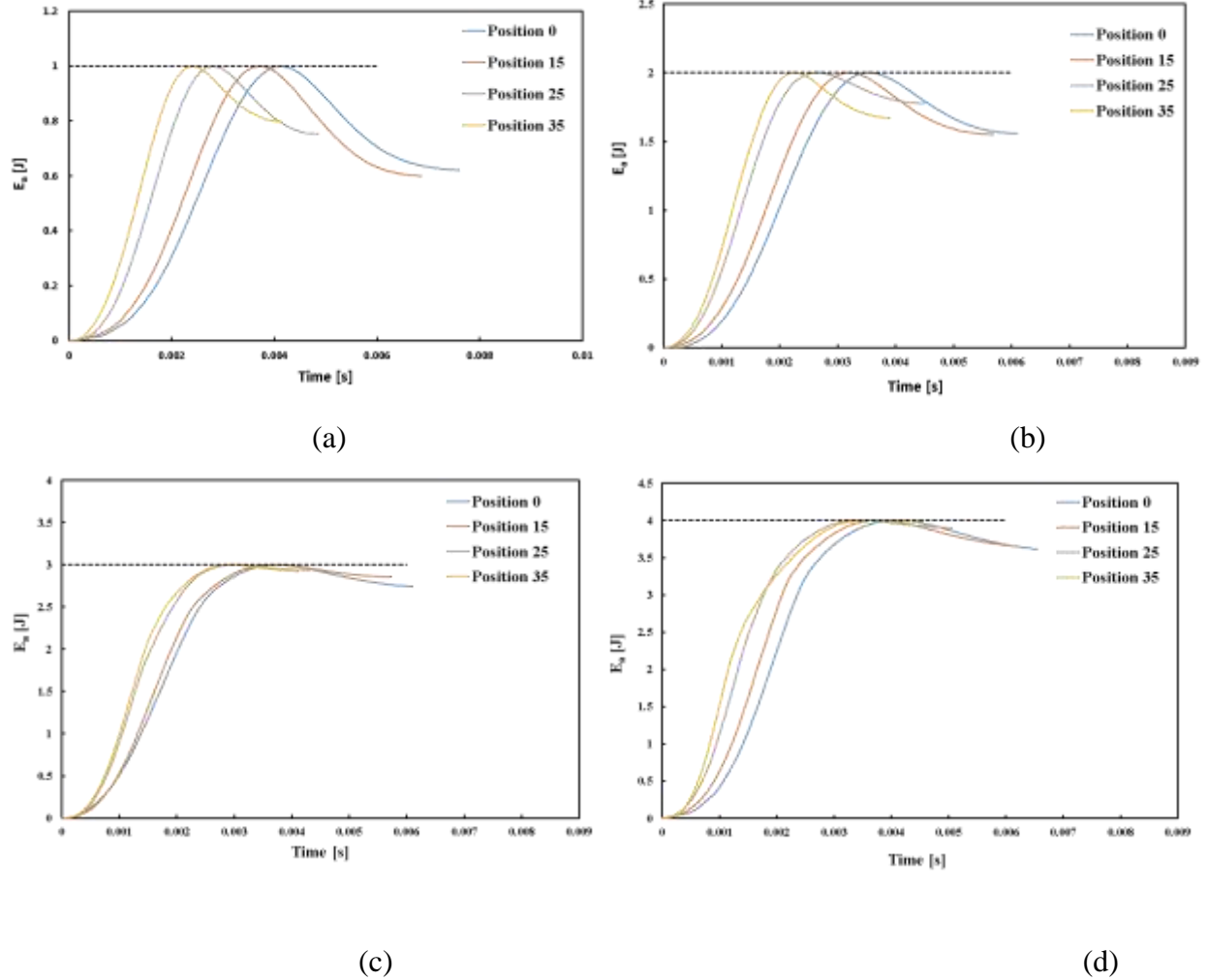
Figure 5. Energy profile for the laminates investigated impacted at different positions, (a) 1 J, (b) 2 J, (c) 3J and (d) 4 J, respectively.

The energy absorbed permanently by the laminates for each impact scenario, as calculated by subtracting the recovered strain energy from the total transferred kinetic energy, are presented in Figure 6a which indicates that the laminates absorb more energy with increasing impact energy. For example, panels impacted centrally at 1 Joule absorb only 0.6 Joules compared to 3.6 Joules to those impacted at 4 Joules. Similarly, Figure 6b, indicates a marginal increase in the absorbed energy with respect to increasing the distance from the centre for positions up to 25mm , However,

at 35mm the absorbed energy appears to fall off somewhat which suggests that this position may be influenced by the proximity of two orthogonal boundaries at the corner of the clamped boundary.

| (a) | (b) |
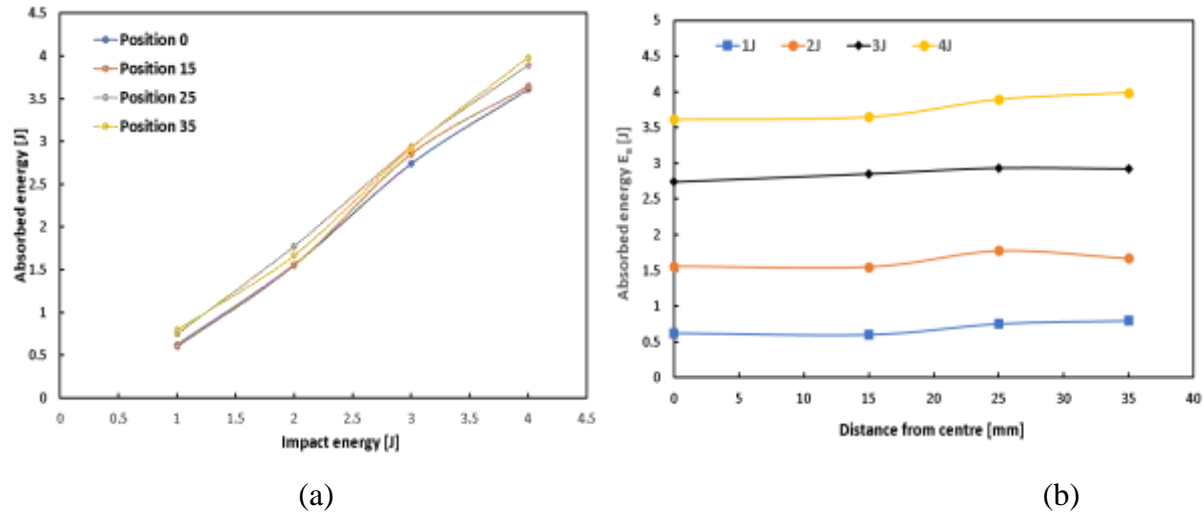
Figure 6. Absorbed energy versus impact energy (a) and impact locations (b) for the laminates investigated.

The results in Figure 6 are presented in a normalized non-dimensional form as percentages of the initial kinetic energy in   (b)

Figure 7. It is demonstrated that panels impacted at center and off-center locations exhibited almost a similar trend at which the absorbed energy percentages increase up to 91.3 %, 95.1 %, 97.8 % at a maximum impact energy of 3 Joules for impact positions of 0, 15 and 25, respectively. However, panels impacted at the 35mm position exhibit the highest energy absorption at impact energy of 4 J with values of 99.6 %, highlighting again the severity of the conditions at which different failure modes are involved in absorbing the kinetic energy of the impactor (i.e., delamination, deformation, matrix cracking and fiber breakage).

(a)   (b)
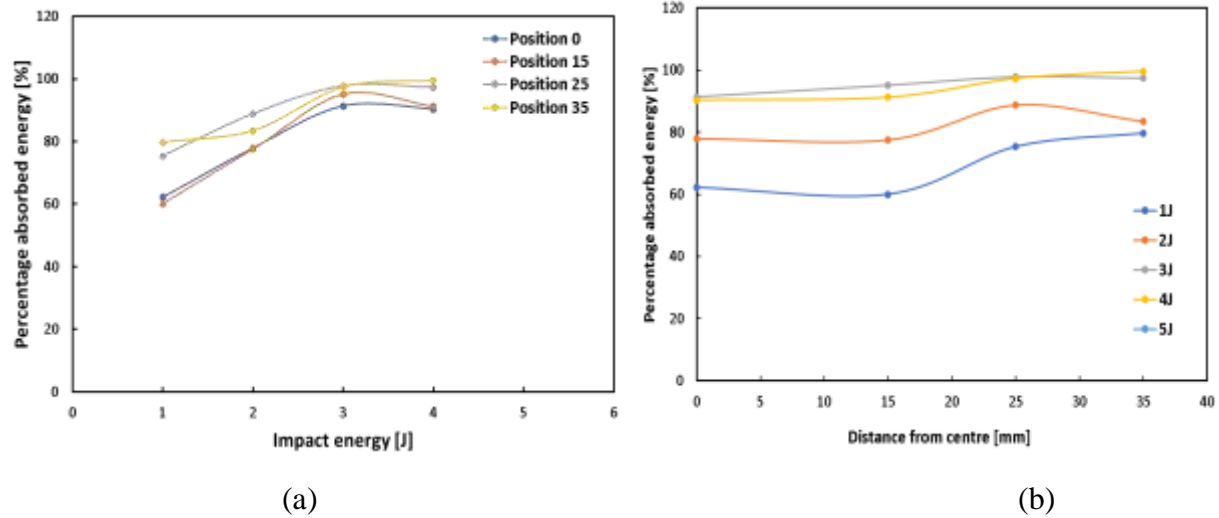
Figure 7.Percentage absorbed energy versus impact energy (a) and impact locations (b) for the laminates impact at the four energy levels.

A digital photographic technique was used to assess the amount of damage occurring around the site of an impact on the laminate panel specimens. The transparent nature of these thin glass fibre-based laminate specimens meant that this area could be examined and measured easily by placing a strong light source behind the panel and looking its silhouette. This process was facilitated further by using a Panasonic camcorder (HDC-SD90, resolution of 2592×1944 pixels) and Image J public domain image analysis software (National Institutes of Health, USA) to map and assess the area of damage. Images showing the evolution failure of the impacted laminates over the four energy levels four different locations are presented in Figure 8. The proximal faces (impacted side), shown in Figure 8a, show the delamination and matric cracking, whereas the distal faces, shown in Figure 8b, highlighted the fibre breakage. Clearly, the severity of the damage of the impacted laminates increases with impact energy and at impact positions away from the centre towards the boundary.
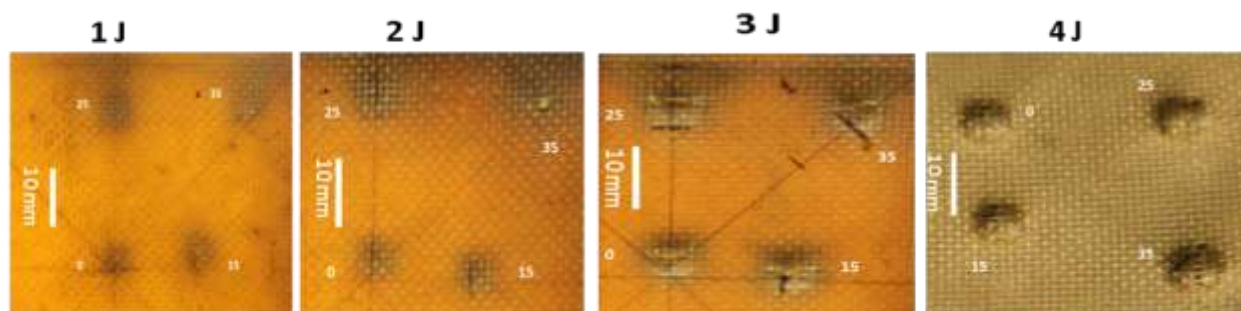
(a)
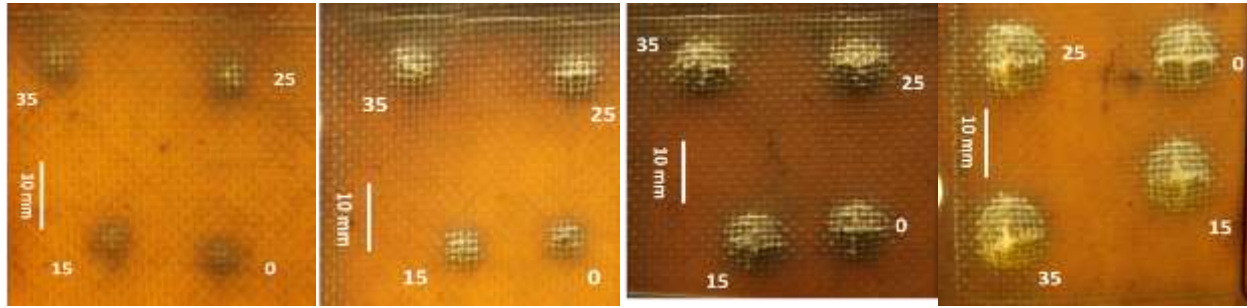
(b)

Figure 8. Photographs of the panels investigated subjected to impact at different energies and different locations, (a) the front face, (b) the back face.

The damage area vs. impact energy and impact position are shown in Figure 9a and Figure 9b, respectively. It can be noted from Figure 9a that the damage areas increase with impact energy in all impact locations. For example, the failure areas of panels impacted at 1 Joule at the 0mm and 35mm positions are 33.5 mm^2 and 91.2 mm^2, respectively, compared to 50.8 mm^2 and 116 mm^2, respectively, for the corresponding panels impacted at 4 Joules. It was also observed that laminates impacted near the boundary exhibit almost linear behavior, whereas, non-linear trend was noticed for those impacted at central and near central locations. An examination of Figure 9b indicates that the values of damage area show a high dependency on impact position with the near boundary position exhibiting the largest damage area compared to those impacted at central position. For example, the failure area of laminated impact centrally at 1 Joule, 2 Joules, 3 Joules and 4 Joules are 33.5 mm^2, 43.2 mm^2, 74.4 mm^2 and 91.2 mm^2, respectively, compared 50.8 mm^2, 74.9 mm^2, 97.5 mm^2 and 116.1 mm^2 for those impacted at the 35 off-centre position for the same impact energy.

(a)   (b)
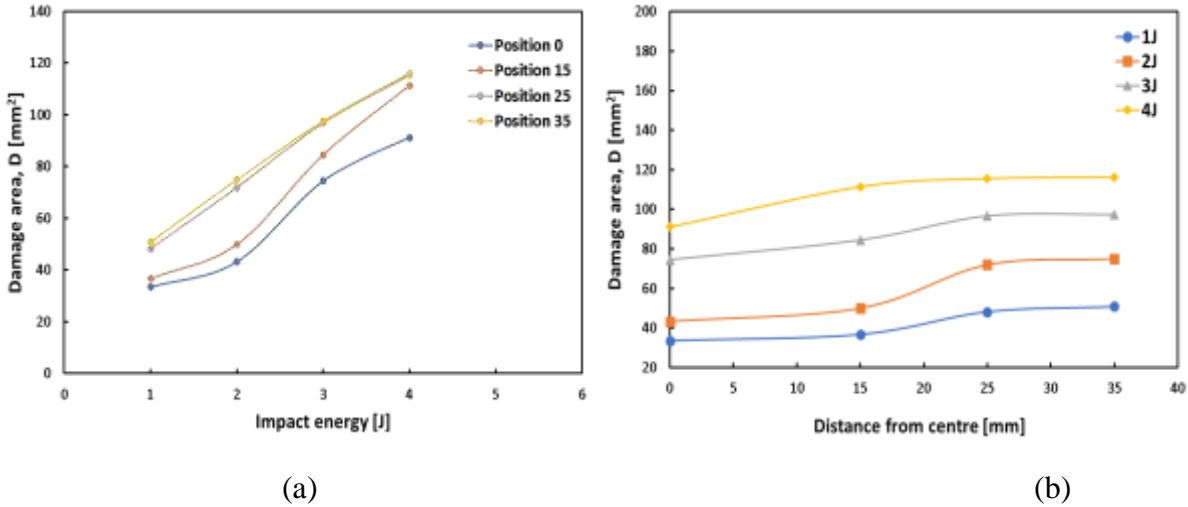
Figure 9. Damage area around the impact site with respect to (a) impact energy and (b) impact position for the various impact energies considered.

4.1 Finite element model

The response of the laminate panels subjected to central and off-centre impacts was examined using the ABAQUS/Explicit finite element analysis (FEA) software. This analysis focused initially on investigating the force vs. time histories for the various impact scenarios. A comparison between the measured force vs. time curves derived from the experimental data at 1 Joule impact energy and the corresponding FEA model prediction for different off-centre impact locations is shown in Figure 10. It is clear from this figure that the predictions from the FEA model correlate well with the experimental results in terms of the characteristic increase in force to a maximum followed by a rapid fall-off to zero. The results indicate that the FEA models are capable to capture the main fundamental features for the laminates investigated subjected to impact near boundary locations.

(a)   (b)   (c)
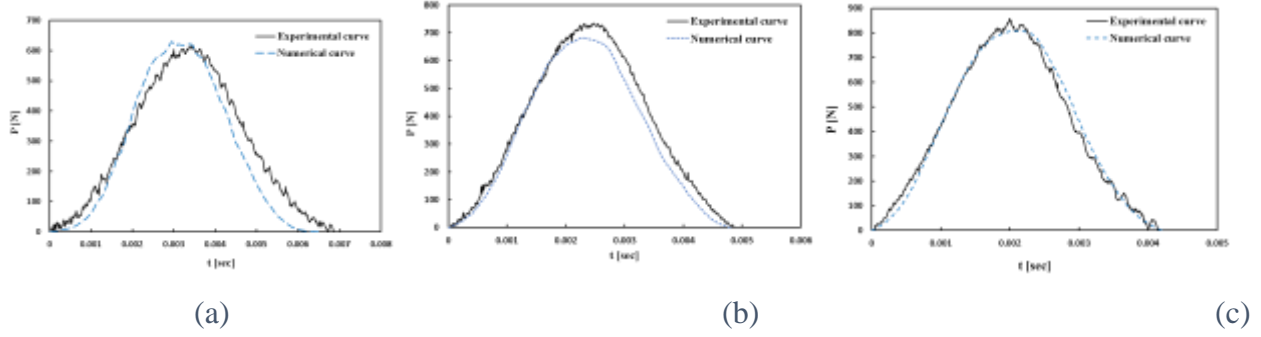
Figure 10. Experimental and FEA force vs. time profiles for the panels investigated impacted at positions (a) 15mm; (b) 25mm and (c) 35mm with an impact energy of 1 Joule.

To further investigate the validity of the numerical model, a comparison between the predictions for peak forces and maximum displacements from the FEA model and the experimental data is made in Figure 11. A closer examination of this figure indicates that the predictions from the FEA model tend to underestimate the actual peak force slightly (Figure 11a) and overestimate slightly the maximum displacement (Figure 11b). However, overall, the results from the FEA model are in a good agreement with the experimental data.

(a)   (b)
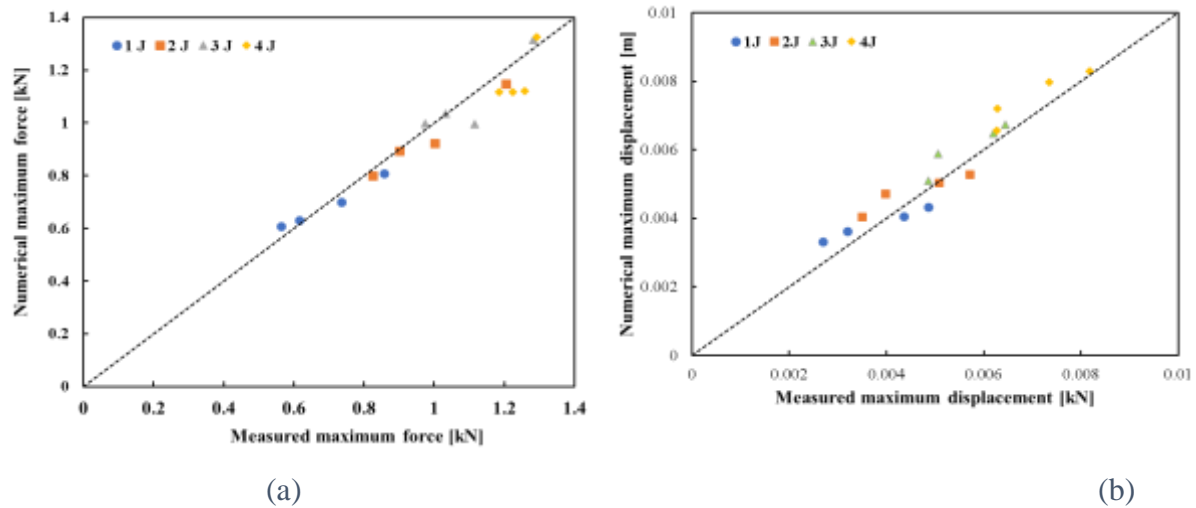
Figure 11. Comparison of the results from the FEA model for (a) maximum force and (b) maximum displacement with measured experimental data.

Figure 12 compares the impact damage from the experiment with the prediction from the FEA model for laminates impacted centrally and at the 25mm position with 1 Joule impact energy. It can be seen from the figure that the FEA model predicts the damage at center position well. The cross-sectional option available in ABAQUS is used here to highlight the damage evolution through the panels during impact event and shows the delamination between the first three plies while the others are not affected by this relatively low impact energy. However, the impact at the 25mm position, shown in Figure 12b, indicates damage in all plies of the laminate and indicates they all participate in absorption process. In turn, this highlights the severity of the impact at positions near to the boundary condition. It is also shown that values for the maximum Von Misses stress decrease at position away from the centre. For example, the approximate maximum Von Misses stresses for laminates impacted centrally and at the 25mm position are 330MPa and 93MPa, respectively.

(a)   (b)
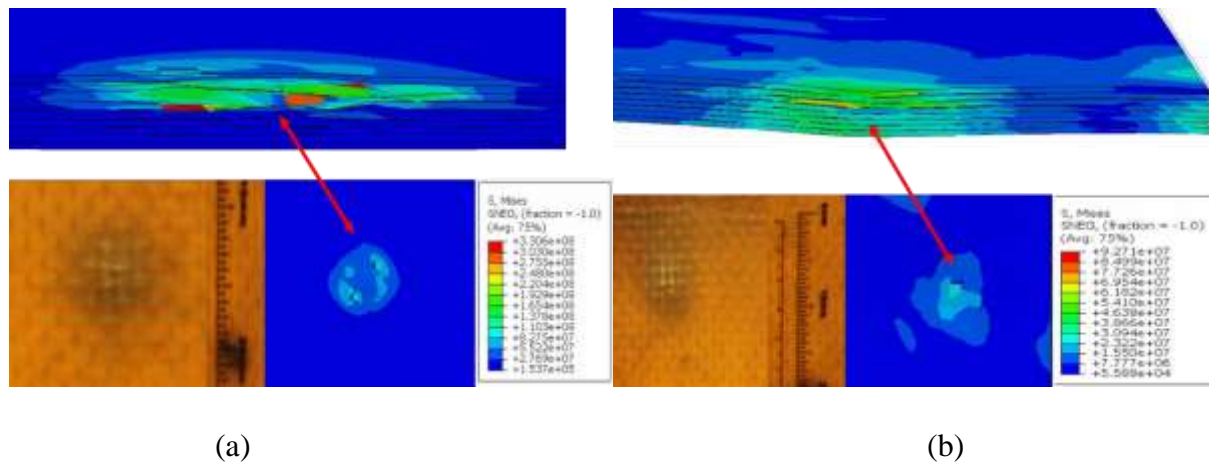
Figure 12. Comparison between experimental and FEA model predictions for laminate damage at sites impacted with 1 Joule at the (a) centre and (b) 25mm positions.

Further validation of the FEA model was carried out by modelling impacts at the centre position considering the 4 Joules impact energy case and comparing these results with the corresponding experimental data. A summary of this comparison is provided in Figure 13 which shows that the FEA analysis provides a good prediction of the cross-shaped damage that occurred in the experimental test. Again, a cross-section of the impact site shows the impact energy absorbed

locally by the laminate through its different damage modes, i.e., delamination, matrix cracks and fibre breakage

.
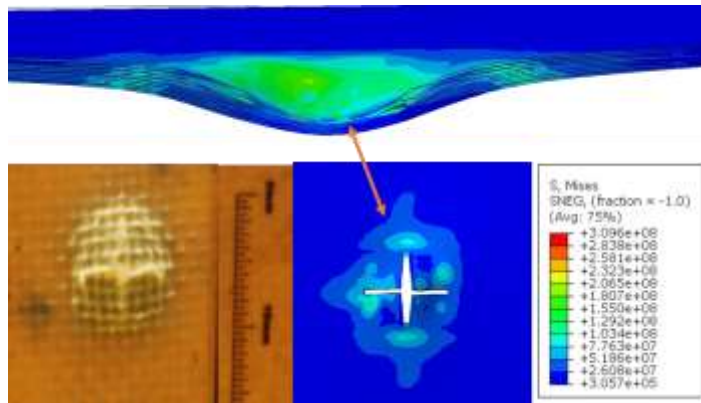
Figure 13. Experimental and numerical damage modes for laminates impacted at 4 Joules at the central position.

Figure 14 shows the predicted damage modes from the FEA model for the cases of an impact at 3 Joules at the 0 mm, 15 mm, 25 mm and 35 mm positions. Again, the results show the values of the maximum Von Mises stress reduces with increasing distance from centre which are, approximately, 374 MPa, 357 MPa, 265 MPa, and 170 MPa for these four impact positions, respectively. The cross-sectional area of the laminate at each of these impact sites are provided in Figure 15 a-d which, when compared with the cross sectional areas in Figure 13, indicate the number of layers involved in absorbing energy increases with respect to increasing impact energy and the distance from centre.

(a)   (b)

(c)   (d)
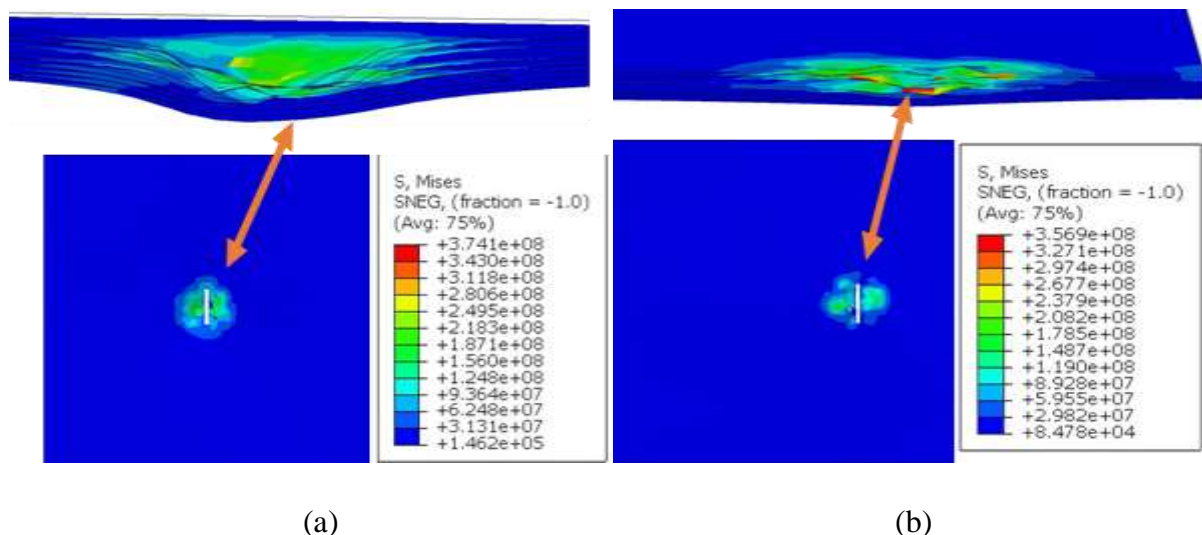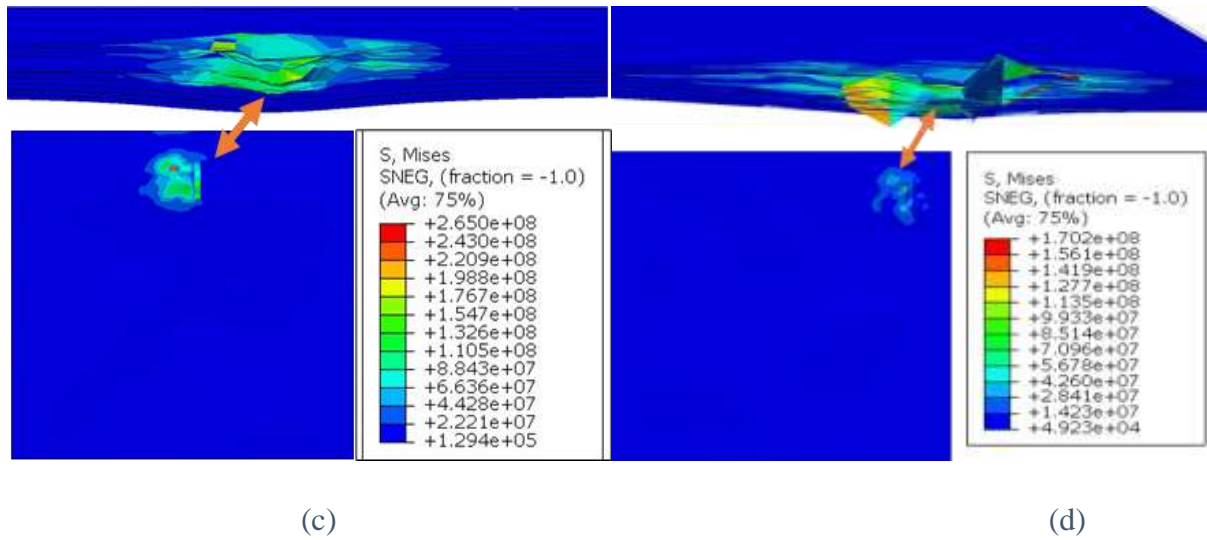
Figure 14. FEA model predicted damage cross-sections for laminates investigated impacted with 3 Joules at the (a) 0 mm, (b) 15 mm (c) 25 mm and (d) 35 mm positions.
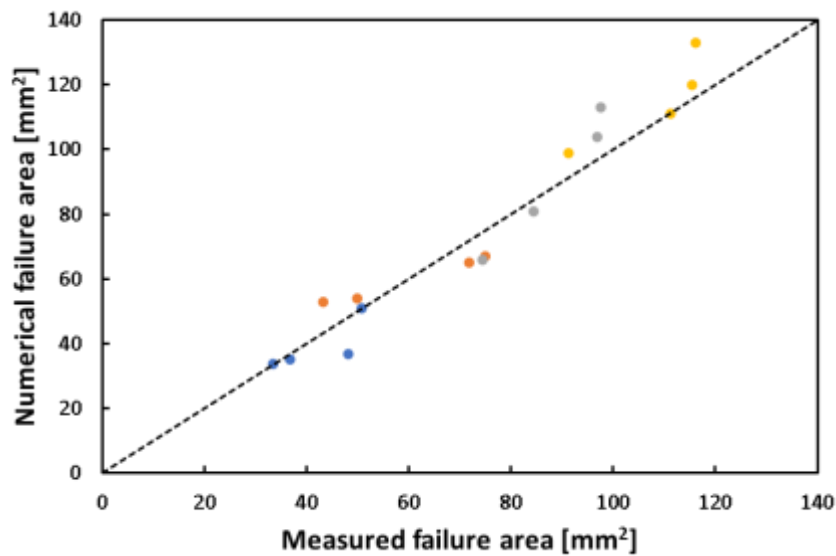
Figure 15 - Experimental measured damage area vs. damage area predicted by the FEA model for all target positions and impact energies.

LVI tests on the CFRP sandwich panels having Nomex honeycomb core (this part is present in Mecsol 2024 another version of this work will be improved to be published as a journal paper)

Pouria Bahrami and Marcilio Alves

Group of Solid Mechanics and Structural Impact, Department of Mechatronics and Mechanical Systems Engineering, University of Sao Paulo, Sao Paulo 05508900, Brazil.

Abstract: This study investigates the performance of honeycomb sandwich composite panels under low-velocity impact (LVI) and their residual flexural strength. The panels, featuring a Nomex hexagonal core and plain weave carbon fiber-reinforced composite skins, were subjected to low-impact energies using a drop-weight rig. Following each impact, a beam segment encompassing the impacted area at the mid-span was extracted from the sandwich panel. This segment underwent a quasi-static three-point bending test to evaluate the residual flexural strength of the sandwich panel postimpact. A finite element model of the impact was developed using the Abaqus/Explicit solver. The results showed good agreement between the numerical model and experimental tests, validating the accuracy of the finite element analysis.
Keywords: Nomex core, Sandwich panel, Low-impact velocity, 3-point bending, Residual strength.

1   INTRODUCTION

Honeycomb sandwich composite structures feature a lightweight honeycomb core between two thin, laminated face sheets. Widely used in bus, airplane, ship, and train structures for their high specific strength and stiffness, composite sandwich panels may suffer from low impact resistance due to the thin outer face sheets. Damage tolerance is more complex than in conventional laminated structures, involving not only matrix failure, fiber fracture, and delamination but also core damage. Understanding their behavior under low-velocity impact (LVI) is crucial for advancing their applications.

In recent decades, numerous researchers have experimentally investigated composite sandwich structures with a honeycomb core under low-speed normal impact loads (Dear et al., 2005; Dogan & Arikan, 2017; Herup & Palazotto, 1998). Additionally, numerical modeling techniques have increasingly become essential for studying and designing these structures, as they significantly reduce the number of trials and associated resource costs.

The CFRP/Nomex sandwich panels are being widely used in airplane structures like rudders. They consist of carbon/epoxy composite face sheets and a Nomex honeycomb core. Both the face sheets and the core are orthotropic and exhibit varied failure modes depending on strain rates and impact angles at the mesoscale. In some instances, the sandwich panel may experience core failure without visible damage to the face sheets, known as barely visible impact damage (BVID). This type of damage can lead to complex internal structural failures, significantly reducing the residual strength of the composite, and it is difficult to detect through routine nondestructive examinations (Song et al., 2021).

The impact response of CFRP/Nomex sandwich panels has been extensively investigated both numerically and experimentally (Chen et al., 2018) and continues to be a subject of significant interest among engineers. In this study, low-velocity impact (LVI) tests on a sandwich panel were conducted to (i) investigate the post-LVI residual strength of the impacted samples and (ii) evaluate the performance of a finite element (FE) model based on an elastic material response to predict damage on CFRP face sheet and Nomex core.

2   EXPERIMENTAL AND NUMERICAL STUDIES Experiments

Figure 1 illustrates the drop hammer test rig and setup for the low-velocity impact (LVI) tests on the sandwich panels. The sandwich panel was secured to a plate holder with a central hole of 100 mm in diameter, using four toggle clamps to hold the specimen in place. Since the damage to the CFRP and the core did not propagate far from the impact region, multiple impact tests were conducted on a single sample. The samples were impacted by a hemispherical indentor with a diameter of 25 mm, at energies of 4 and 7 Joules. After the LVI tests, beam samples were cut from the sandwich panel such that the impact damage was located in the middle of the beams. The

dimensions of the sandwich panels, along with the mechanical properties of the CFRP face sheet, interface, and Nomex core, are listed in Tables 1-4.
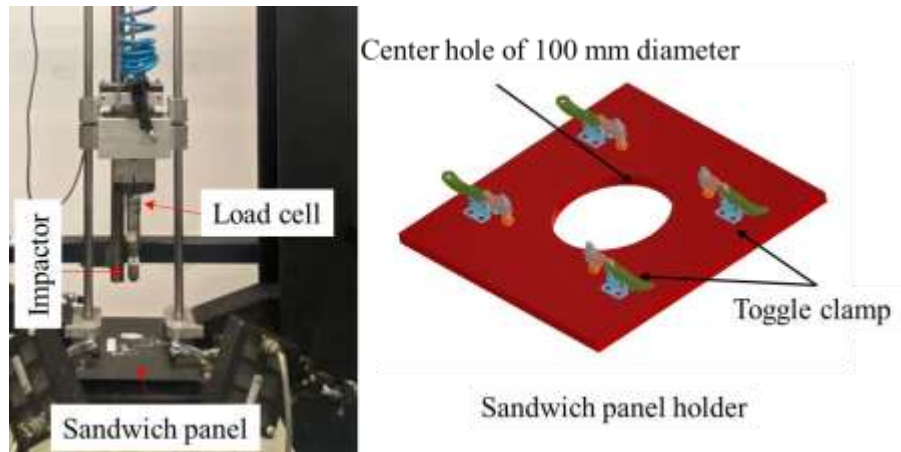

Figure 1 – Impact test setup.

Table 1 - Dimension of sandwich panels.

Feature	Material	Thickness (mm)	W×L (mm²)
Face sheet	Four layers of PW CFRP	0.239×4	270×270
Core	Nomex honeycomb	12.604	

Table 2. Mechanical properties of Nomex material (Seemann & Krause, 2017).

Properties	Symbol	Unit	Value
Elastic modulus 1-direction	E_1	GPa	5.00
Elastic modulus 2-direction	E_2	GPa	4.00
Shear modulus	G_{12}	GPa	1.45

Poisson's ratio	μ	-	0.2
Tensile strength 1-direction	XT	MPa	90
Tensile strength 2-direction	YT	MPa	60
Compressive strength 1-direction	XC	MPa	105
Compressive strength 2-direction	YC	MPa	90
Shear strength	S	MPa	44
Density	ρ	kg/m^3	1100
Single layer thickness	t	mm	0.051
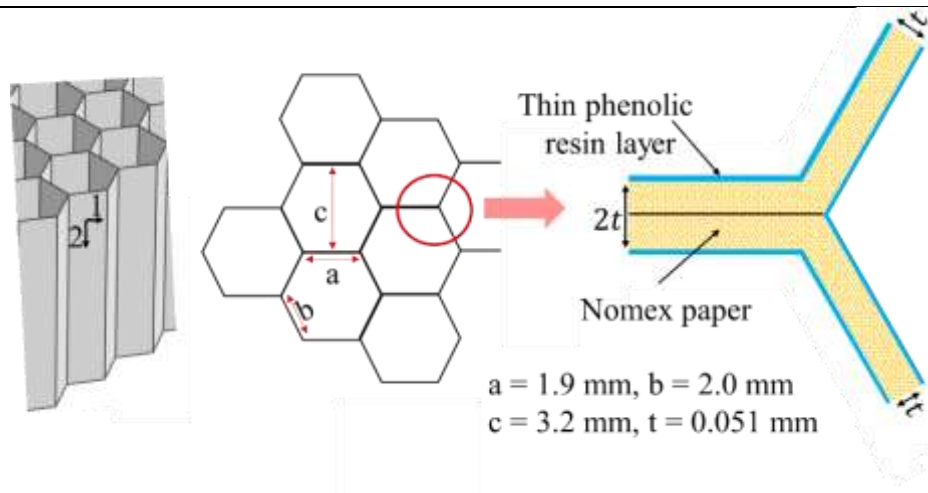
Table 3 - Mechanical properties of CFRP fabric.

Properties	Symbol	Unit	Value
Warp elastic modulus, 1-direction	$E1$	GPa	50.2
Weft elastic modulus, 2-direction	E_2	GPa	50.2
Elastic modulus, the thickness direction	$E3$	GPa	9.60

Shear moduli	*G12, G13, G23*	GPa	2.5
Poisson's ratios	μ	-	0.13
Tensile strength (warp) 1-direction	*XT*	MPa	687
Tensile strength (fill) 2-direction	*YT*	MPa	
Compressive strength (warp) 1-direction	*XC*	MPa	564
Compressive strength (fill) 2-direction	*YC*	MPa	
Compressive strength 3-direction	Z^C	MPa	340 [23]
Shear strength	*S, S13 *, S23**	MPa	94
Density	ρ	kg/m^3	1440
Ply thickness	*t*	mm	0.239

Table 4 - Mechanical properties of interface

	t_n0	64
Peak strength (MPa)	t_s0	84
	t_t0	84
	G_n	0.8
Critical fracture toughness (N/mm)	G_s	1.5
	G_t	1.5
	K_n	3000
Penalty stiffness (N/mm^3)	K_s	3000
	K_t	3000

Note: The cohesive property parameter η= 1.45 is selected.

3 Numerical analysis

The response of the CFRP woven fabric plies is considered and modeled as an equivalent orthotropic elastic material until failure onsets, implemented through a VUMAT user-material subroutine in Abaqus/Explicit code. For composite materials, there are several failure theories such as Hashin's criteria (Hashin, 1980; Hashin & Rotem, 1973) and those presented by Hou et al. (Hou et al., 2000), that consider two different failure mechanisms; fiber failure modes (in the 1direction) and matrix failure modes (in the 2-direction). The failure theories mentioned are well-suited for unidirectional composite tapes, where mechanical properties in the fiber direction (1-direction) are controlled by the fibers, while properties and failure mechanisms in the transverse direction (2-direction) predominantly rely on matrix behavior. In this study, the woven fabric features an equal distribution of fibers in both in-plane orthogonal directions, resulting in the reinforcement of both directions (1 and 2) with fibers. Additionally, in alignment with references (López-Puente et al., 2003, 2008), a few adaptations were made to existing failure theories: (I) the incorporation of fiber failure criteria for both in-plane directions and (II) the exclusion of analogous matrix crushing and matrix cracking as seen in the model proposed by Hou et al. (Hou et al., 2000).

The stress-based failure variables, denoted as d_i and expressed in Equations 1-4, have been established to account for various failure modes. These modes include fiber failure (d_{f1}, d_{f2}), in-plane shear failure (d_{m12}), and out-of-plane crushing (d_{m3}) (Artero-Guerrero et al., 2014). The values of these failure variables can either be zero (indicating no damage) or one (the initiation of damage). When a damage variable reaches a value of one, the corresponding stress components are reduced to zero. The combination of the damage variables and the element deformation gradient was employed as a criterion for the element removal scheme, as outlined in the reference (Ataabadi et al., 2022).

3.1 Finite element model

A finite element (FE) model for simulating low-velocity impact on composite plates is developed using the Abaqus/Explicit commercial finite element software. The laminated composite plate is modeled by stacking multiple layers of continuum plies, allowing the simulation

to capture both intralaminar and interlaminar responses during impact. This layered FE approach is designed to accurately predict the detailed mechanical behavior of composite plates under low-velocity impact conditions. The built-in surface-based cohesive model in Abaqus is employed to represent the inter-layer mechanical response.

Figure 1 illustrates the selected mechanical behavior of the composite ply. In the non-progressive damage response, the material exhibits elastic behavior (path AB) until the failure criterion is reached at point B. At this stage, the mechanical properties associated with the failure mode are instantaneously reduced to 90% of their initial values. Following this degradation, the failed element undergoes a near-complete unloading process (path BC) while remaining active in the simulation. This mechanical response is applied to composite plies in the in-plane directions (directions 1 and 2) as well as in the through-thickness direction (Z-direction) under both compressive and tensile stress conditions. To prevent excessive distortion of the failed element, an element deletion criterion is employed. Once this criterion is satisfied (point D), the failed element is removed from the simulation.

Fig. 1. Bilinear stress-strain response of inter-layer composite ply.

3.2 Intralamina response

A three-dimensional stress state user material subroutine (VUMAT) is employed to simulate the orthotropic behavior of composite plies. The stress-strain relationship for this 3D stress state is described by Eq. 1

$$
\begin{bmatrix} \sigma_{11} \\ \sigma_{22} \\ \sigma_{33} \\ \sigma_{12} \\ \sigma_{23} \\ \sigma_{13} \end{bmatrix} =
\begin{bmatrix}
C_{11} & C_{12} & C_{13} & & Zeros & \\
 & C_{22} & C_{23} & & & \\
 & & C_{33} & & & \\
 & & & 2C_{44} & & \\
 & Sym & & & 2C_{55} & \\
 & & & & & 2C_{66}
\end{bmatrix}
\begin{bmatrix} \varepsilon_{11} \\ \varepsilon_{22} \\ \varepsilon_{33} \\ \varepsilon_{12} \\ \varepsilon_{23} \\ \varepsilon_{13} \end{bmatrix}
\tag{1}
$$

By introducing appropriate damage variables, that degrade the components of the stiffness matrix Eq.1 will represent the material's response under both intact (undamaged) and damaged conditions regarding the value of the corresponding damage variables. Consequently, the general form of the stiffness matrix components is presented in Eq. 2.

$$C_{11} = (1 - d_f)C_{11}^0 \tag{a}$$
$$C_{22} = (1 - d_f)C_{22}^0 \tag{b}$$
$$C_{33} = (1 - d_m)C_{33}^0 \tag{c}$$
$$C_{12} = (1 - d_f)(1 - d_m)C_{12}^0 \tag{d}$$
$$C_{23} = (1 - d_f)(1 - d_m)C_{23}^0 \tag{e}$$
$$C_{13} = (1 - d_f)(1 - d_m)C_{13}^0 \tag{f}$$
$$G_{12} = (1 - d_f)(1 - d_{mc})C_{44}^0 \quad , C_{44}^0 = G_{12} \tag{g}$$
$$G_{23} = (1 - d_f)(1 - d_{mt})(1 - d_{mc})C_{23}^0 \quad , C_{55}^0 = G_{23} \tag{h}$$
$$G_{13} = (1 - d_f)(1 - d_{mt})(1 - d_{mc})C_{13}^0 \quad , C_{66}^0 = G_{13} \tag{i}$$

(2)

There are two types of damage variables in Eq. 2; (I) fiber dominant damage variables (d_f) and (II) matrix dominant damage variables (d_m). In this study, the same amount of fibers are placed in two in-plane orthogonal directions of GFRP composite (1-direction and 2-direction), thus, d_{f1} and d_{f2} are fiber damage variables due to fiber failure modes in 1-direction and 2-direction, respectively. Besides fiber dominant failure modes, the composite plies can fail due to matrix damage failure modes where matrix damage variable d_m degrades the corresponding components of stiffness matrix as expressed in Eq.2. All damage variables are defined in Eq. 3.

$$d_{f1} = 1 - (1 - d_{f1t})(1 - d_{f1c}) \tag{a}$$
$$d_{f2} = 1 - (1 - d_{f2t})(1 - d_{f2c}) \tag{b}$$

(3)

$$d_f = 1 - (1 - d_{f1})(1 - d_{f2}) \tag{c}$$

$$d_m = 1 - (1 - d_{mt})(1 - d_{mc}) \tag{d}$$

Note: The subscripts c and t denote compression and tension failure modes, respectively.

The initial (undamaged) components of the stiffness matrix, C_{ij}^0, in Eq. 2 are calculated using the formulas provided in Eq.4.

$$C_{11}^0 = E_{11}(1 - v_{23}v_{32})\Delta \tag{a}$$

$$C_{22}^0 = E_{22}(1 - v_{13}v_{31})\Delta \tag{b}$$

$$C_{33}^0 = E_{33}(1 - v_{12}v_{21})\Delta \tag{c}$$

$$C_{12}^0 = E_{11}(v_{21} - v_{31}v_{23})\Delta \tag{d}$$

$$C_{13}^0 = E_{11}(v_{31} - v_{21}v_{32})\Delta \tag{e}$$

$$C_{23}^0 = E_{22}(v_{32} - v_{12}v_{31})\Delta \tag{f}$$

$$\Delta = \frac{1}{(1 - v_{21}v_{12} - v_{32}v_{23} - v_{13}v_{31} - 2v_{13}v_{21}v_{32})}$$

$$\tag{4}$$

The material model incorporates six independent damage variables (d_{mt}, d_{mc}, d_{f1t}, d_{f1c}, d_{f2t}, d_{f2c}) under compressive and tensile loading conditions. All fiber and matrix dominant damage variables can take one of two values: (I) zero, representing the undamaged condition, and (II) a maximum value ($d_{max} = 0.90$) when the damage criterion is met when a damage variable turns equal to 0.90 it will remain constant during the simulation. In other words, the material exhibits linear elastic behavior until a failure criterion is satisfied, at which point the corresponding damage variable instantaneously reaches its maximum value. Consequently, the associated components of the stiffness matrix are degraded by Eq. 2.

Six failure criteria are employed to account for intralaminar damage. As previously mentioned, for plain weave GFRP composite plies under investigation, an equal amount of fibers is present in both the 1- and 2-directions. Therefore, unlike unidirectional plies, fiber damage (due to compression and tension) is considered in both the 1- and 2-directions. Matrix failure modes

under compression and tension are also taken into account to characterize damage in the out-of-plane (Z-direction). All failure modes are detailed in Eq. 5.

Fiber failure tension in i-direction ($i=1,2$)	$f_{ft}^i = \left(\dfrac{\sigma_i}{X_i^T}\right) + \left(\dfrac{\tau_{12}}{S_{12}}\right) + \left(\dfrac{\tau_{i3}}{S_{i3}}\right) \geq 1$	(a)
Fiber failure compression in i-direction ($i=1,2$)	$f_{fc}^i = \left(\dfrac{\sigma_i}{X_i^C}\right) + \left(\dfrac{\tau_{12}}{S_{12}}\right) + \left(\dfrac{\tau_{i3}}{S_{i3}}\right) \geq 1$	(b)
Matrix failure tension out-of-plane direction	$f_{mt} = \left(\dfrac{\sigma_3}{Y_z^T}\right) + \left(\dfrac{\tau_{13}}{S_{13}}\right) + \left(\dfrac{\tau_{23}}{S_{23}}\right) \geq 1$	(c)
Matrix failure compression out-of-plane direction	$f_{mc} = \left(\dfrac{\sigma_3}{Y_z^C}\right) + \left(\dfrac{\tau_{13}}{S_{13}}\right) + \left(\dfrac{\tau_{23}}{S_{23}}\right) \geq 1$	(d)

(5)

To prevent excessive distortion of failed elements, an element deletion criterion is implemented in the VUMAT code. The decision to remove an element from the simulation is based on the ratio of the element's current volume to its initial volume. Through a process of trial and error, the upper and lower thresholds for this ratio were determined to be 1.85 and 0.55, respectively.

3.3 Interlaminar response

A surface-based cohesive model with a traction-separation law is employed between adjacent composite plies to simulate the interlaminar cohesive response in the laminated plate. This approach is commonly used in numerical simulations of composite structures. For conciseness, only the key features of the interface model are summarized in Table 1.

Table 1. Cohesive surface features.

Traction-separation law	$\begin{Bmatrix} t_n \\ t_s \\ t_t \end{Bmatrix} = \begin{bmatrix} E_{nn} & 0 & 0 \\ & E_{ss} & 0 \\ Sym & & E_{tt} \end{bmatrix} \begin{Bmatrix} \varepsilon_n \\ \varepsilon_s \\ \varepsilon_t \end{Bmatrix}$
Damage initiation criterion	$max \left\{ \dfrac{\langle t_n \rangle}{t_n^0}, \dfrac{t_s}{t_s^0}, \dfrac{t_t}{t_t^0} \right\} = 1$

|	
Damage evolution	$$d = \frac{\delta_m^f(\delta_m - \delta_m^0)}{\delta_m(\delta_m^f - \delta_m^0)}$$
Mixed mode propagation criterion	$$G^C = G_n^C + (G_s^C - G_n^C)\left\{\frac{G_s}{G_T}\right\}^\eta$$

The Nomex core is considered an elastic orthotropic material and an in-built progressive failure model for composite materials in Abaqus is used to simulate this response. The material properties of Nomex are presented in Table 2.

4   RESULTS

Figure 2 illustrates the force-time history of the 4J and 7J impact tests on the sandwich panel. For both impact scenarios, the elastic (undamaged) response of the sandwich panels is very similar. However, after reaching the maximum impact force, the panel subjected to the 7J impact exhibited a longer plateau force, which was primarily carried by the Nomex core, supported by the back face sheet. In both conditions, the back face sheet remained intact.

.
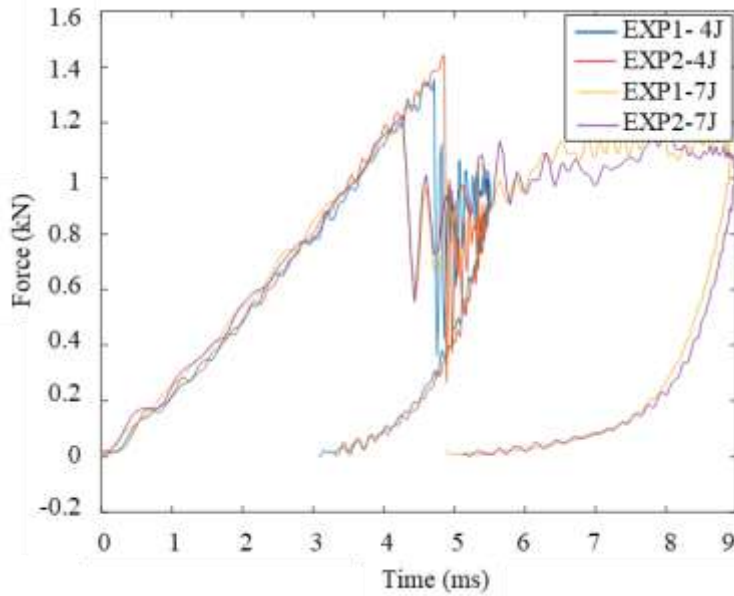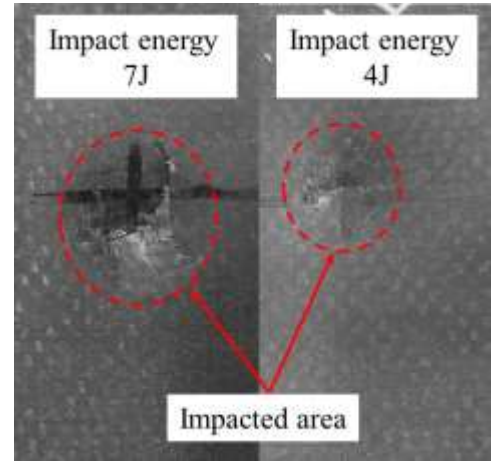
(a)   (b)

Figure 2 – LVI test results; (a) Force-time curves of LVT tests on sandwich panels and (b) Permanent indentation on the CFRP upper face sheet.

Figure 3 shows the results of the 3-point bending tests. As expected, the impact-induced damages decreased the flexural bending strength of the sandwich beams cut from the panels. However, a remarkable reduction was not observed in the force-displacement curves between the intact beams and the impacted ones. Additionally, the difference in maximum force between the beams impacted with 4J and 7J energy was not evident in Figure 3.
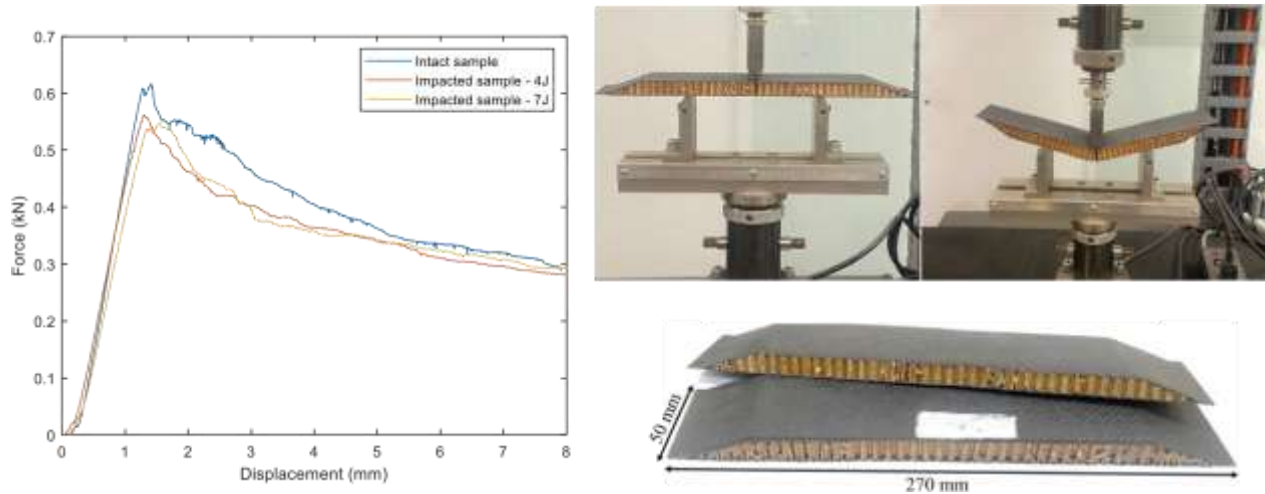
Figure 3 – The results of 3-point bending for intact and damaged beam specimens.

Figures 4 and 5 compare the numerical and experimental impact forces and impact-induced damage on the sandwich panels subjected to 7J impact energy. Although the numerical model predicted the impact force in the undamaged region with reasonable accuracy (with improved material calibration, a much better agreement between the experimental and numerical models could be achieved), the unloading responses of the numerical model and the experimental test, as well as the depth of permanent indentation on the upper CFRP face sheet, are significantly different. The finite element (FE) model failed to accurately predict the rebounding process, as it is based on an elastic-damage response and is not well-suited for capturing inelastic deformation. In this model, it is assumed that the Nomex core exhibits an elastic response until the point of damage initiation.

(a)   (b)
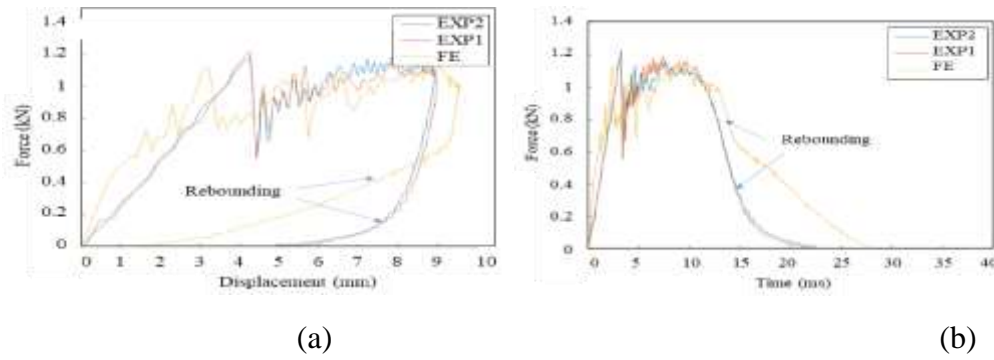
Figure 4 – Results of 7J impact on sandwich panel; (a) Force displacement and (b) Force-time history.
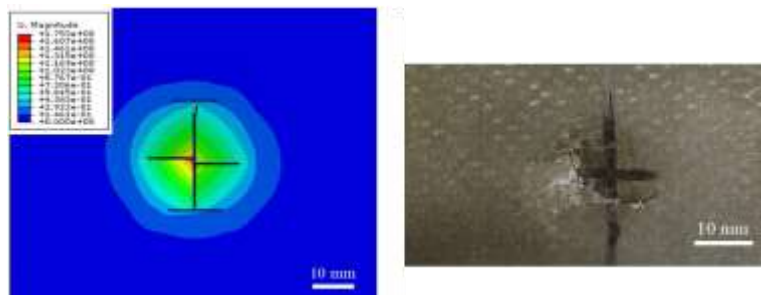
Figure 5 – Damage and permanent indentation on the CFRP face sheet of the sandwich panel (7J impact test).

5   CONCLUSIONS

The low-velocity impact response of CFRP/Nomex sandwich panels was investigated both experimentally and numerically. Impact-induced damages undermine the bending strength of the sandwich panel; however, for impact energies of 4J and 7J, the reduction in strength was not remarkable. In the numerical model, both the CFRP face sheets and the Nomex core were treated as elastic orthotropic materials. However, the finite element (FE) model was unable to accurately predict the unloading process and the permanent indentation on the sandwich panels. This discrepancy is primarily due to the significant differences in the mechanical properties of the CFRP and Nomex core; the carbon/epoxy face sheets are brittle, whereas the Nomex core is ductile. Therefore, a material model capable of incorporating the inelastic response of the materials is required for accurately modeling the CFRP/Nomex sandwich panels.

The shortcomings of the code and numerical model in accurately predicting the rebound path in the force-displacement curves for both GFRP laminates and sandwich panels are evident. Although this is a well-known issue in the literature, we aim to address it by considering various possibilities, such as the inelastic response of GFRP and sandwich panels, including plastic deformation and related phenomena. Efforts to improve this aspect will continue, representing a valuable contribution to the field of low-velocity impact (LVI) testing of composite materials.

Experimental Study on the Hygrothermal and Thermal Effects on the Crashworthiness of CFRP Laminated Composites

The scope of this study includes the following:

1. **Environmental Conditioning and Material Aging**
   - Controlled exposure of CFRP laminated composite specimens to thermal and hygrothermal environments in order to simulate aging conditions typically encountered in service.
   - Thermal aging is performed at elevated temperatures (e.g., 50 °C and 75 °C), while hygrothermal aging involves immersion in distilled water at controlled temperatures (e.g., 25 °C and 75 °C) over extended durations.
   - Additional post-aging treatments (e.g., redrying) are employed to evaluate the reversibility of moisture-induced degradation.

2. **Axial Impact Testing of Aged CFRP Tubes**
   - Fabrication and preparation of CFRP tubes with different stacking sequences (e.g., cross-ply and angle-ply configurations).
   - Execution of quasi-static compression and drop-weight impact tests to assess crashworthiness metrics such as energy absorption means crushing force, and specific energy absorption (SEA).
   - Comparison between unaged, aged, and re-dried specimens to isolate the effects of moisture uptake and thermal softening on mechanical performance.

3. **Failure Analysis and Crash Mode Evaluation**
   - Detailed examination of failure mechanisms through post-impact inspection, including identification of macroscopic crushing modes and inter/intralaminar failure characteristics.
   - Analysis of the influence of stacking sequence and environmental degradation on the stability and deformation patterns during axial impact loading.

4. **Correlation with Material Degradation Mechanisms**
   - Interpretation of results based on known matrix degradation phenomena, such as plasticization, fiber-matrix debonding, and reduced interlaminar shear resistance due to moisture diffusion and thermal exposure.

o   Discussion of how environmental effects alter the balance between fiber-dominated and matrix-dominated failure modes.

Experimental assessment of effects of elevated temperature and hygrothermal aging on the axial impact response of CFRP laminated tubes (submitted to Polymer Composite Journal)

Abstract

This study investigates the effects of elevated temperature and moisture absorption on the crushing response of carbon fiber-reinforced polymer (CFRP) tubes under dynamic axial compression. Tubes with cross-ply and angle-ply lay-ups, fabricated from the same unidirectional CFRP/epoxy material, were tested to evaluate how thermal and hygrothermal preconditioning influences crashworthiness. Two environmental conditions were applied: (i) elevated temperature exposure (50 °C and 75 °C), and (ii) hygrothermal aging, involving water immersion at 25 °C and 75 °C for 50 days. Dynamic impact tests were performed using a drop-weight setup at ~6 m/s. A subset of the hygrothermally aged tubes (75 °C) was re-dried at 40 °C for 3 days to assess the reversibility of moisture-induced degradation. Aged and unaged tubes were compared based on macroscopic failure modes and crashworthiness indicators, including specific energy absorption (SEA) and mean crushing force. Results show that both elevated temperature and hygrothermal exposure reduce crashworthiness, with temperature effects being more severe. While no significant changes were observed in the macroscopic crushing modes, signs of increased ductility were noted. The re-dried specimens confirmed that hygrothermal aging causes permanent mechanical degradation. Stacking sequence significantly influenced moisture uptake: at 75 °C, angle-ply tubes absorbed ~30% more moisture than cross-ply tubes. Moreover, the stacking sequence affected stability under axial impact, with cross-ply tubes exhibiting superior impact performance at elevated temperatures. This was attributed to their fiber-dominated crushing mechanism, which is less sensitive to matrix degradation than the matrix-dependent response of angle-ply tubes.

1. Introduction

Fiber-reinforced polymer (FRP) composites are widely used in various engineering applications due to their high strength-to-weight ratio, excellent corrosion resistance, and versatility in design. However, their performance can be significantly affected by environmental conditions, such as elevated temperatures and moisture. The combined influence of temperature and humidity, referred to as hygrothermal aging, can degrade the mechanical properties of FRP composites, leading to potential failures in structural applications [1], [2], [3]. Thus,

Elevated temperatures can soften the polymer matrix within the composite, reducing its load-bearing capacity and altering its viscoelastic properties. At the same time, moisture absorption can cause swelling, microcracking, and matrix-fiber debonding, weakening the material's structural integrity. The diffusion of water molecules into the polymer matrix can also lead to plasticization, further reducing stiffness and strength [1]. Thermal and hygrothermal effects are particularly relevant for applications exposed to harsh environments, such as aerospace, marine, and automotive sectors, where materials are subjected to fluctuating temperature and humidity conditions over extended periods. Understanding how thermal and hygrothermal aging affects FRP composites is crucial for predicting their long-term performance, developing more durable materials, and designing structures that can withstand these environmental challenges.

The synergic effects of thermal and hygrothermal degradation on the mechanical properties of composite materials under various loading conditions (such as low-velocity impact and tensile loading) have been extensively studied in the literature. These investigations have been conducted on different composite components, including coupon samples, plates, sandwich panels, and tubes. In the present work, the focus is on the impact loading on tubular composite components. Therefore, previous studies investigating the effects of hygrothermal conditions on the impact

response of composite structures with plate and tube geometries are reviewed. For a more comprehensive review of hygrothermal effects on composite materials, readers are referred to Refs.[4], [5].

Hygrothermal influence on the mechanical properties of CFRP/GFRP Sandwich Composites is investigated in Ref. [6]. This study examines moisture absorption and its impact on open-edge vs. encapsulated sandwich composites exposed to water at 25°C, 50°C, and 74°C. Results indicate that synthetic foam cores of the sandwich panels absorb significantly more moisture than CFRP/GFRP skins, leading to severe strength reduction in foam specimens, partially reversible through redrying. Encapsulated sandwich panels show superior durability and residual strength, while open-edge configurations tend to fail by core shear under prolonged hygrothermal exposure. Impact damage depth increases for moisture-exposed sandwich beams, but damage size remains mostly unaffected.

In Refs. [7], [8], the impact performance of CFRP plates with different stacking sequences, subjected to water immersion and freeze cycles, was investigated. The findings indicate that moisture absorption enhances impact resistance. As moisture interacts with the resin, it weakens Van der Waals forces and hydrogen bonding, leading to increased epoxy ductility. This change allows laminates with higher moisture content to dissipate more impact energy through elastic deformation. However, statistical analysis suggests that variations in lay-up configurations have a negligible effect on moisture absorption and impact performance.

In Ref. [9] CFRP laminated plates aged for three months in a climate chamber (70°C, 85% relative humidity) before undergoing low-velocity impact tests. The study reports that energy absorption increases with aging time, suggesting that matrix degradation alters the failure mechanisms. Initially, aged composites exhibit brittle behavior, but with prolonged exposure, matrix plasticization, and moisture diffusion enhance energy dissipation, improving impact resistance over time.

Investigation on impact response of carbon fiber/epoxy laminates with different stacking sequences after being submerged in distilled water at 80°C for up to 35 days [10] indicates that unidirectional laminates absorb more moisture than cross-ply or quasi-isotropic configurations, affecting their impact performance. Higher moisture content reduces impact impulse and increases strain during loading, suggesting increased ductility due to matrix softening. In contrast to Refs.

[7], [8], the study highlights the need to consider laminate design when evaluating moisture resistance in impact applications.

According to the above-mentioned publications, hygrothermal exposure negatively affects composite materials' integrity through resin weakening, degrading their mechanical properties. However, while this degradation adversely affects composite components, it paradoxically enhances energy absorption by increasing the material's ductility and ability to dissipate impact energy. However, some publications indicate hygrothermal conditions can worsen the LVI performance of composite plates. For instance, Ref. [11] investigates the effects of hygrothermal aging on the single and repeated low-velocity impact (LVI) response of glass/epoxy composites, exposing samples to 95°C and 75% humidity for up to 1300 hours. Aging reduced impact resistance due to thermo-oxidative degradation, leading to surface deterioration, microcracks, and polymer chain scission. In repeated impacts, aged samples exhibited a threefold decrease in absorbed energy until perforation.

A ballistic impact study on CFRP laminated composites [12] demonstrates that the ballistic limit velocity of hygrothermally aged composites decreases due to moisture-induced weakening of the matrix and fiber-matrix interface. This reduction in impact resistance is attributed to the degradation caused by moisture absorption, which compromises the structural integrity of the composite and diminishes its ability to withstand extreme loading conditions.

In contrast to studies on LVI tests, the limited researches on axial quasi-static compression of tubes after hygrothermal aging consistently show that hygrothermal exposure negatively impacts the energy absorption capacity of composite tubes. The crashworthiness of CFRP tubes subjected to elevated temperatures (70°C, 100°C, 160°C) and long-term water immersion at 25°C and 70°C is investigated in Ref. [3]. The findings indicate that thermal and hygrothermal conditions significantly degrade the energy absorption capacity and mechanical integrity of the tubes. The loss of interfacial adhesion and matrix softening due to moisture absorption likely contribute to this reduction in crashworthiness. In Ref. [13] the effects of prolonged exposure to water at 55°C, 65°C, and 75°C (for up to 40 days) on the axial compressive strength of glass fiber-reinforced composite pipes are studied. The results show that higher temperatures and longer aging durations lead to a progressive decline in strength, indicating moisture penetration and matrix degradation.

This degradation likely weakens the fiber-matrix interface, reducing load transfer efficiency and leading to early failure under compression.

The stacking sequence plays a crucial role in determining the mechanical properties of composite materials. The effect of hygrothermal aging on the mechanical performance of composite samples with different stacking sequences has been investigated in the literature. For instance, Ref. [14] studied the impact of long-term (over 15 months) seawater aging on unidirectional, cross-ply, and multidirectional carbon fiber-reinforced polymer (CFRP) coupon specimens subjected to compressive loading. The findings indicated that the stacking sequence significantly influences the compression failure mode after prolonged hygrothermal exposure. Specifically, it is reported that the residual compressive strength of cross-ply and multidirectional laminates decreased by approximately 50% after long-term aging, whereas the reduction observed in unidirectional specimens was around 28%.

This study explores the crashworthiness of thermally and hygrothermally aged CFRP tubes under axial impact loading, focusing on the influence of aging conditions on their energy absorption capabilities. To evaluate the effect of lay-up configuration, two different stacking sequences were analyzed to determine their role in moisture absorption behavior and crashworthiness parameters, such as specific energy absorption (SEA) and mean crushing force. Additionally, a set of aged samples was re-dried to assess whether the adverse effects of hygrothermal aging are reversible. The findings aim to provide insights into how environmental exposure affects the structural integrity and impact resistance of CFRP tubes with different stacking sequences, which is critical for their application in energy-absorbing structures.

2. Material and aging processes

2.1 Material

Two cylindrical tubes, each with an inner diameter of 50 mm, were fabricated from unidirectional carbon fiber-epoxy prepregs using two different stacking sequences: a cross-ply stacking sequence $[0/(90)_2/0]_s$ and an angle-ply stacking sequence $[\pm 45/0/\pm 45/0/\pm 45/0/\pm 45]$. Samples with an initial length of 120 mm were cut from the tubes, with one end cut flat at 90° and the other end externally beveled at 45° as a crush trigger mechanism as shown in Fig.1(a). The dimensions of the tubes and the mechanical properties of the unidirectional CFRP are provided in Table 1.

Table 1. Tubes' dimensions and mechanical properties of CFRP unidirectional layer [14].

Tubes' dimensions			Mechanical properties CFRP	
Feature	CP	AP		
Inner diameter (mm)	50.00	50.00	Elastic modulus E_1 (GPa)	135
			Elastic modulus E_2 (GPa)	10
			In-plan shear modulus G_{12} (GPa)	5
			Major Poisson's ratio v_{12}	0.3
Outer diameter (mm)	54.38	54.70	Tensile strength 1-direction (MPa)	1500
			Tensile strength 2-direction (MPa)	50
Weight per unit length (g/mm)	0.54	0.59	Compressive strength 1-direction (MPa)	1200
			Compressive strength 2-direction (MPa)	250
			Shear strength (MPa)	70

Note 1: CP: Cross-ply tube ([0/(90)$_2$/0]$_s$) and AP: Angle-ply tube ([±45/0/±45/0/±45/0/±45]).

Note 2: To achieve approximately the same thickness for both tubes, a combination of unidirectional plies with areal densities of 300 gsm (0.3 mm thick) and 200 gsm (0.2 mm thick) was used in their fabrication.

Note 3: The 0°, ±45°, and 90° orientations are measured relative to the tube axis.

Note 4: The 1-direction corresponds to the fiber direction, while the 2-direction is transverse to the fiber direction in the unidirectional CFRP.

2.2 Aging processes

Both cross-ply and angle-ply specimens were subjected to thermal and hygrothermal conditions before the impact tests. For each condition, two specimens were prepared for each specific impact test.

2.2.1 Dry thermal processing

The Instron Heatwave thermal chamber, equipped with a sophisticated temperature control system, was used to apply elevated temperatures to the tube specimens. Two groups of specimens were placed in the thermal chamber at 50°C and 75°C for three hours before the impact tests, allowing sufficient time for the specimens to reach uniform thermal equilibrium (thermal chamber is shown

in Fig. 1(b)). However, the impact tests were conducted at room temperature. The time between removing a specimen from the thermal chamber and performing the impact test was kept to a minimum (below 20 seconds) to prevent significant heat loss from the specimens.

2.2.2. Hygrothermal aging

The tubes were submerged in distilled water, and the container was placed in the thermal chamber at a constant temperature. Two groups of specimens were prepared for the hygrothermal aging process: one group was aged at room temperature (25°C), and the other at an elevated temperature (75°C). Tubes were dried at 40°C for two days then the initial weight of each specimen was recorded before the aging process began. During the aging period, the specimens' weight was measured periodically until the process was complete after 50 days. After aging completion, the specimens were removed from the water container and left for approximately five hours to reach room temperature before the impact tests were conducted. The schematic presentation of the hygrothermal environment is presented in Fig. 1(c)
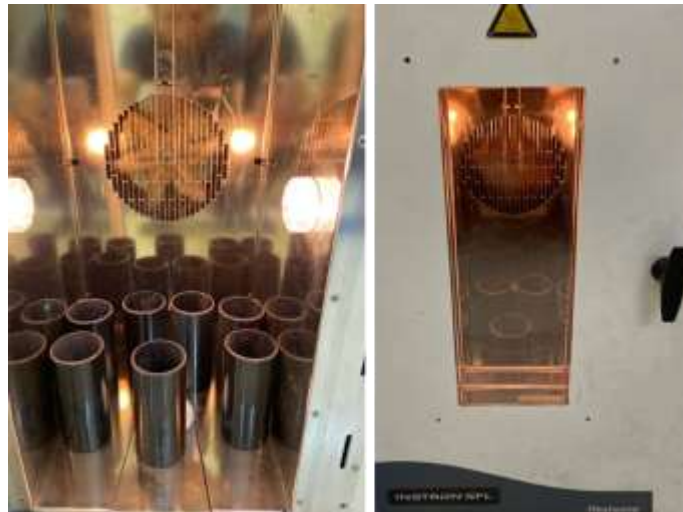
(a)   (b)
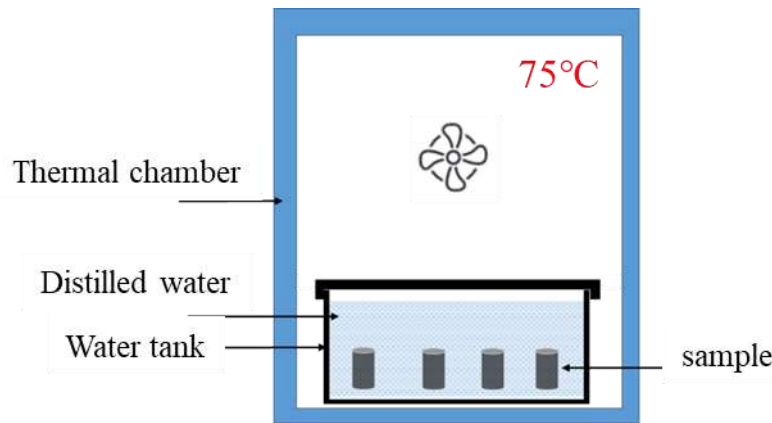
(c)

Fig. 1. Some details of samples and again conditions specimens; (a) CFRP tubes with 120 mm initial length and 45° external bevel, (b) Tubes in the thermal chamber, and (c) Schematic presentation of accelated hygrothermal aging at distilled water.

In addition to the aged specimens, impact tests were conducted on unaged and re-dried specimens that had undergone hygrothermal aging at high temperatures (dried for 72 hours at 40°C in the thermal chamber). This approach was used to evaluate the effects of harsh environmental conditions on the performance of the CFRP tubes through a meaningful comparison. A detailed summary of all samples, including impact energy and aging processes, is provided in Table 2.

Table 2. Summary of CFRP specimens, aging conditions, and impact loading parameters.

Sample ID	Aging/testing condition	Repetition	Impact energy (kJ)
CPU	Unaged - cross-ply tube	2	
CPHG25	Hygrothermal (water immersed @ 25°C) - cross-ply tube	2	
CPHG75	Hygrothermal (water immersed @ 75°C) - cross-ply tube	2	~2.2
CPH50	Elevated temperature 50°C - cross-ply tube	2	
CPH75	Elevated temperature 75°C - cross-ply tube	2	

APU	Unaged- angle-ply tube	2
APHG25	Hygrothermal (water immersed @ 25°C) - angle-ply tube	2
APHG75	Hygrothermal (water immersed @ 75°C) - angle-ply tube	2
APH50	Elevated temperature 50°C - angle-ply tube	2
APH75	Elevated temperature 75°C - angle-ply tube	2
APRD	Re-dried APHG75 samples - angle-ply tube	2

2.3 Impact test procedure

A drop hammer test rig was employed to conduct impact tests on the specimens. An impactor with a mass of 107 kg was released from approximately two meters height above the specimens. The setup was equipped with two high-speed cameras: the first camera, capturing at 20 kfps, recorded the entire impact event and the deformation of the samples under the applied load, while the second camera, operating at 100 kfps, focused on the motion target pattern for further digital image processing and velocity extraction of the impactor, the drop hammer test setup is illustrated in Fig. 2. The extracted velocities were used to calculate the crushing force and crush distance for each specimen. To characterize the crashworthy response of the specimens, several crashworthiness criteria were employed: absorbed energy (E_a), mean crush force (F_m), and specific energy absorption (SEA). These criteria are well-established in the literature; therefore, only their mathematical formulations are presented in Table 3, without further descriptive details.
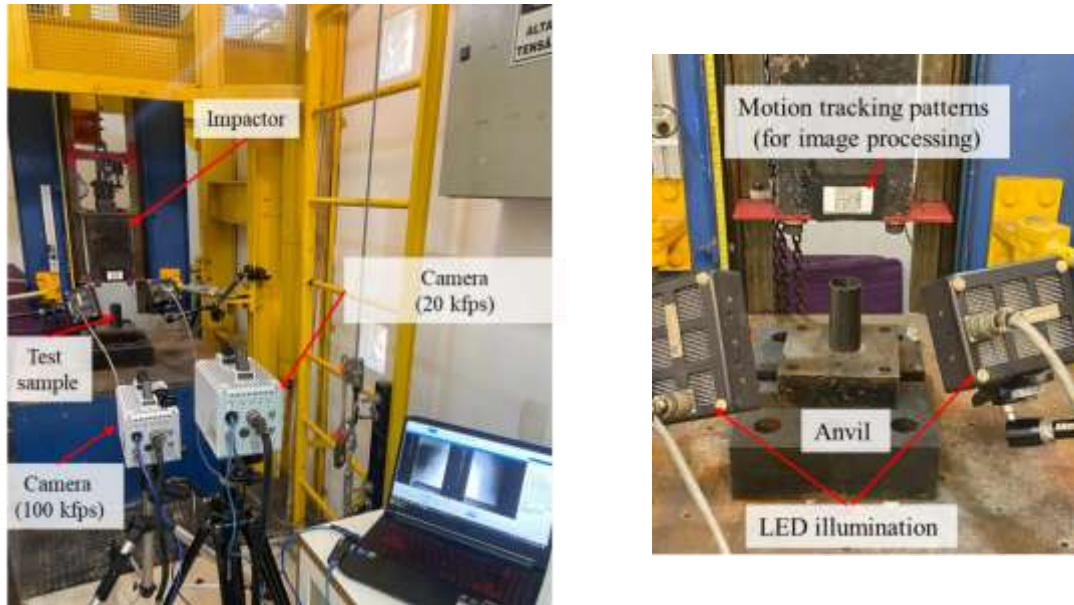
Fig. 2. Impact test setup.

Table 3. Crashworthy criteria.

Criteria	Definition	Calculation
E_a	Absorbed energy (energy dissipated by specimen)	$\int_0^d f\,dx$
SEA	Specific Energy Absorption	$\dfrac{E_a}{m_c}$
F_m	Mean crush force	$\dfrac{E_a}{d}$

f: Crushing force on the specimen

d: Crush distance

m_c: Mass of crushed length of the tube

3. Results and discussion

3.1 Moisture absorption behavior

The moisture absorption of the specimens under hygrothermal conditions was calculated using Eq. 1. The initial dry mass of the specimens is denoted by m_0, while m_t represents the mass at a given

time during the immersion aging period. Moisture uptake at both elevated and room temperatures for the angle-ply and cross-ply specimens was determined using Eq. 1 and is presented in Fig. 3.

$$Moisture\ uptake\ (\%) = \frac{m_t - m_0}{m_0} \times 100 \qquad (1)$$

Figure 3 illustrates the pronounced effect of temperature on accelerating moisture absorption. The water uptake for both cross-ply and angle-ply tubes at 75 °C is substantially higher than that observed at 25 °C. While the difference in moisture uptake between the angle-ply and cross-ply specimens is minimal at 25 °C, at 75 °C the angle-ply specimens exhibit approximately 30% greater absorption than their cross-ply counterparts. These experimental results suggest that the presence of multiple fiber orientations in multidirectional composites provides additional diffusion pathways, thereby increasing the equilibrium moisture content [15]. Table 4 provides a comprehensive summary of the key parameters influencing moisture diffusion, including fiber orientation, the number of resin-rich interfaces, and potential differences in surface finishing conditions. These factors may contribute to the observed variations in moisture uptake between the angle-ply and cross-ply tubes.
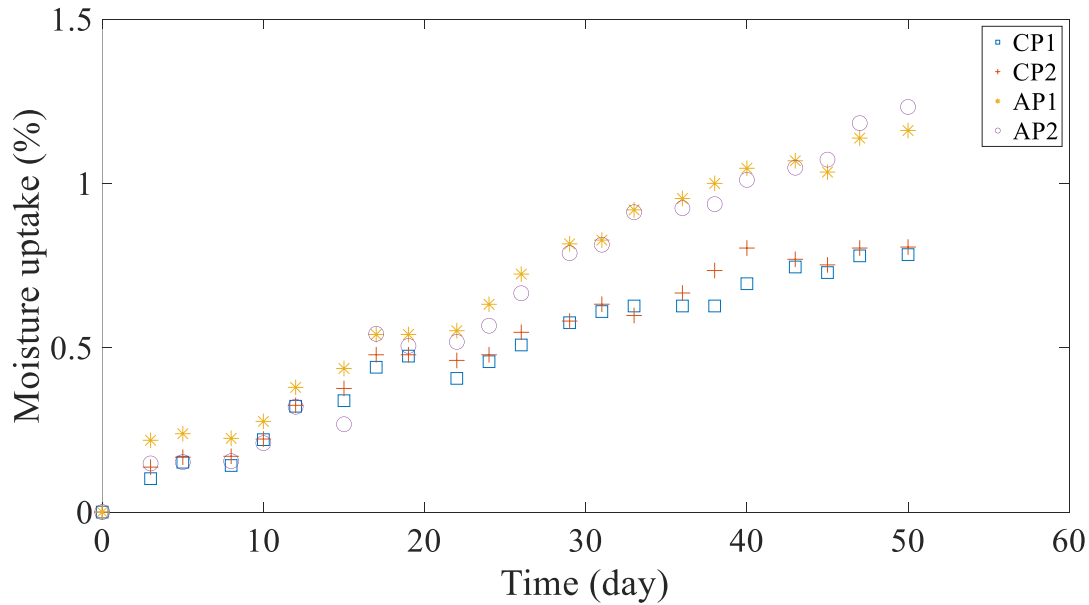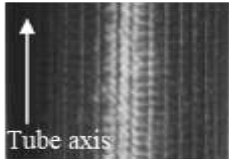
(a)
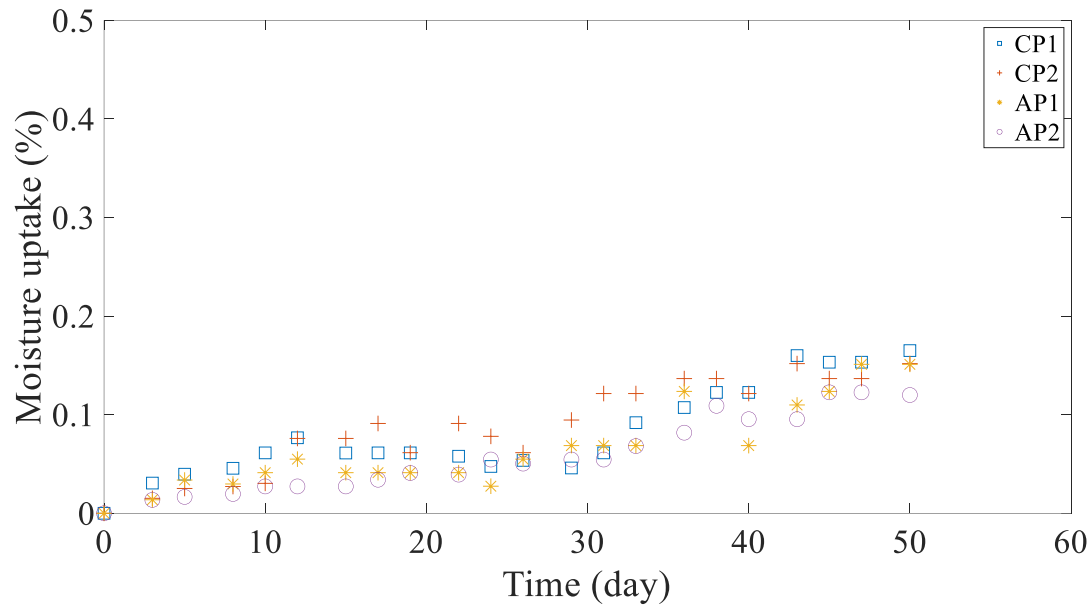
(b)

Fig. 3. Water uptake for cross-ply (CP) and angle-ply (AP) tubes; (a) Tubes immersed at 75°C and (b) Tubes immersed at 25°C.

Table 4. Remarkable physical differences between CP and AP specimens.

Feature		Cross-ply sample	Angle-ply sample
	0°	1 mm	0.6 mm
TF	90°	1.2 mm	0.0
	±45°	0.0	1.6 mm
Number of UD plies		8 (6 layers of 0.3 mm UD and 2 layers of 0.2mm UD)	11 layers of 0.2 mm
Number of resin-rich interfaces		7	10
Outer Surface finishing*			

TF: Total thickness of unidirectional plies in 0°, ±45°, and 90° orientations against the tube axis.

* The inner surface finishing conditions of both angle-ply and cross-ply are the same.

3.2 Effect of aging on the axial crushing response of tubes

This section presents the effect of elevated temperature and hygrothermal conditions on the crushing behavior of cross-ply (CP) and angle-ply (AP) tubes under axial impact load.

3.2.1 Force-displacement and crashworthy metrics

Figure 4 presents the force-displacement curves of angle-ply (AP) and cross-ply (CP) tubes under various environmental conditions. A notable observation is that the crushing forces of the CP tubes are less influenced by hygrothermal and thermal exposures compared to those of the AP tubes. Figure 5 illustrates the average values for specific energy absorption (SEA), crush distance, and mean crushing force for both types of specimens under different aging conditions. Since no consistent trend was observed in the peak loads among the tested samples, the peak load values are not presented here.

Figures 4(a) and 5(a) illustrate the force-displacement curves and selected crashworthiness parameters of the angle-ply specimens under various aging conditions, respectively. In addition to new experimental data, previous impact test results conducted in 2017 and published in 2019 (Ref. [16]) are included for comparison. All tubes were subjected to an impact energy of approximately 2.2 kJ. Due to exposure to thermal and hygrothermal conditions, a reduction in mean crushing force and an increase in crush distance were observed, leading to decreased specific energy absorption (SEA) values compared to unaged specimens.

Among the tested aging conditions, unaccelerated aging (water immersion at room temperature) caused the least significant reduction in the SEA values of the angle-ply tubes compared to unaged tubes (approximately 4%), which aligns with the relatively low water uptake of tubes at room temperature. The effect of thermal conditions at elevated temperatures (50°C and 75°C) on SEA values was more pronounced than the effect of accelerated hygrothermal aging (water immersion at 75°C). Specifically, thermal exposure at 50°C and 75°C led to decreases of 16% and 21% in

SEA values, respectively, whereas accelerated hygrothermal aging at 75°C resulted in a 14% reduction compared to the unaged angle-ply tubes.

The force-displacement responses and the corresponding mean values of the crashworthiness parameters for cross-ply tubes post different aging conditions are presented in Figs. 4(b) and 5(b), respectively. Under both hygrothermal aging conditions (water immersion at 25°C and 75°C), the reduction in specific energy absorption (SEA) values compared to unaged tubes was less than 3%, which is smaller than the reductions observed for the angle-ply specimens. This discrepancy could be attributed to the lower water absorption rates exhibited by the cross-ply specimens compared to the angle-ply tubes. Notably, the SEA reductions for cross-ply tubes impacted at elevated temperatures of 50°C (5% reduction) and 75°C (10% reduction) were substantially smaller compared to those recorded for the angle-ply tubes under similar conditions.
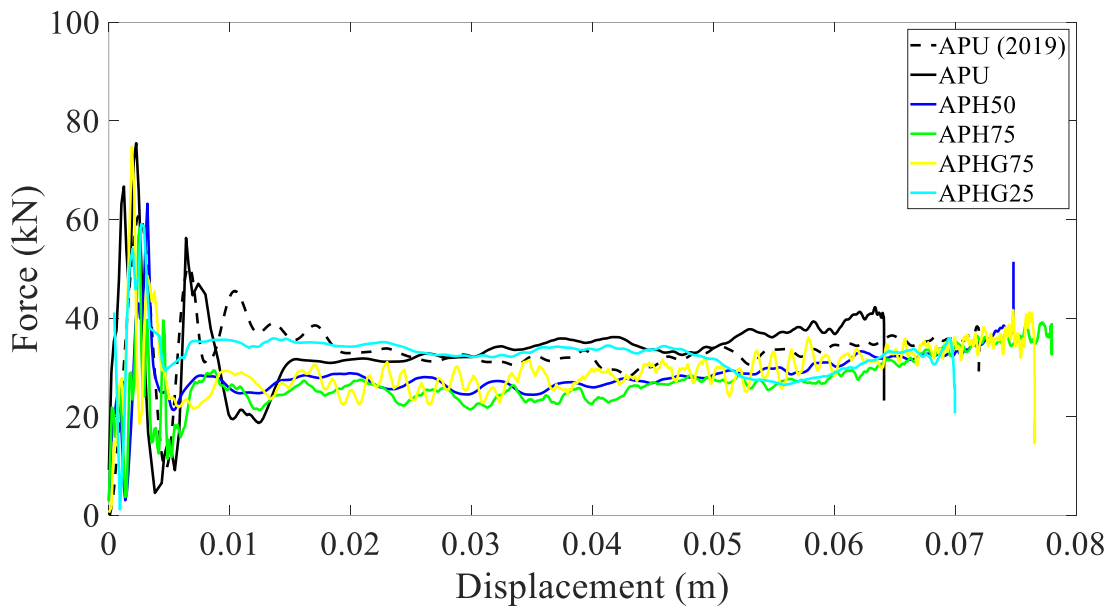
(a)
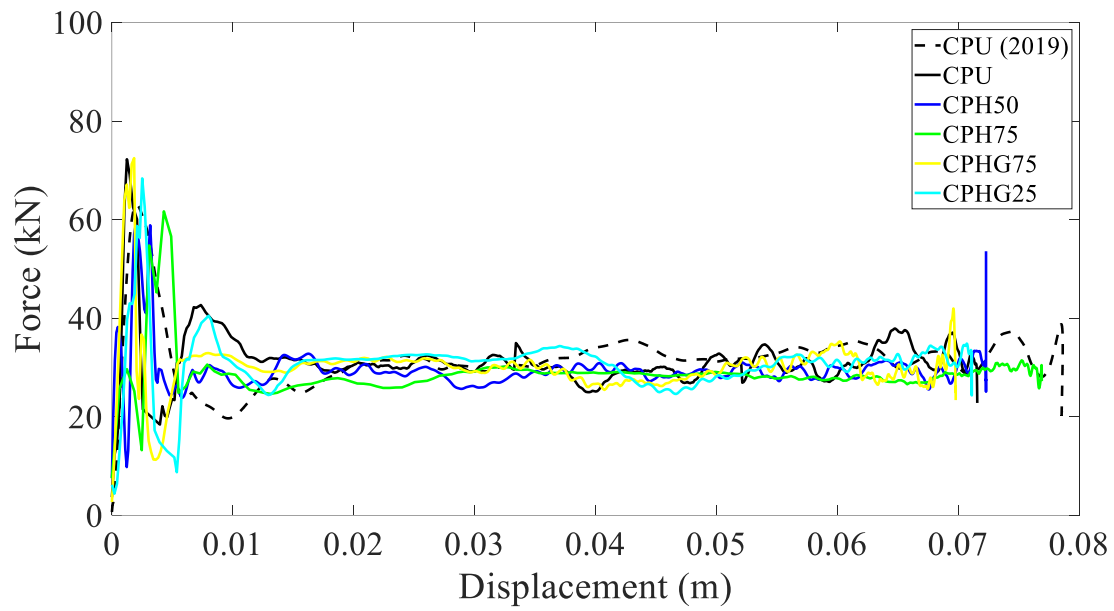
(b)

Fig. 4. Axial crushing force-displacement curves under different environmental conditions: (a) Angle-ply specimens and (b) Cross-ply specimens. Note: After the short initial region near the peak load, a higher level of smoothing/filtering has been applied to the force-displacement curves.
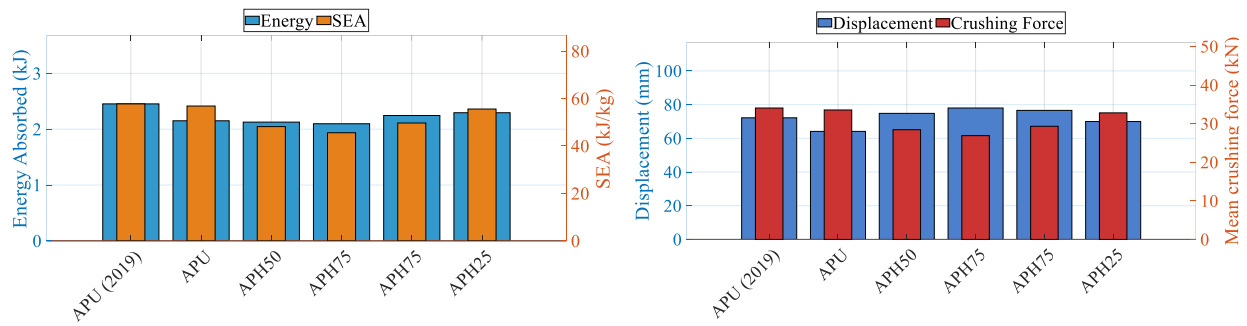
(a)
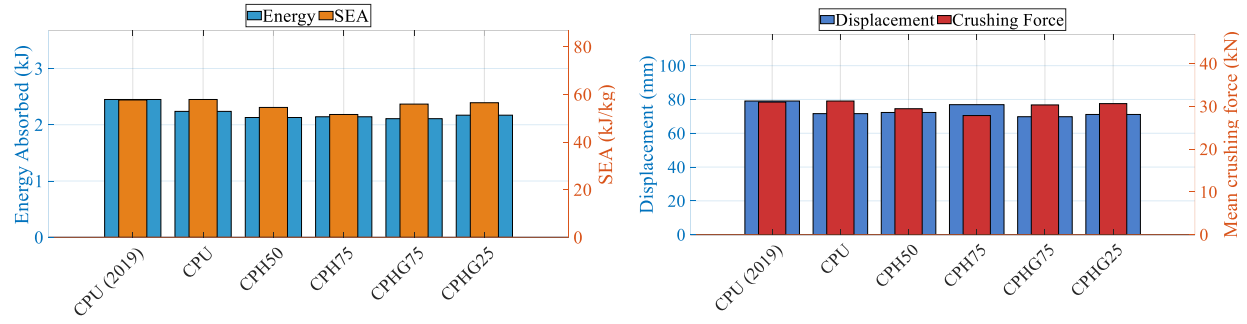
(b)

Fig. 5. Crashworthy metrics for tubes at different aging conditions; (a) Angle-ply tubes and (b) Cross-ply tubes.

Based on the previously discussed differences in impact performance between cross-ply and angle-ply tubes under various aging conditions, it is evident that the cross-ply tubes examined in this study exhibit superior stability under axial impact loading at elevated temperatures. Furthermore, these tubes show enhanced resistance to moisture absorption, which contributes to improved impact performance under hygrothermal conditions. The increased resistance to moisture absorption in the cross-ply tubes, relative to the angle-ply specimens, can be attributed to several factors, including their stacking sequence, the extent of resin-rich interfacial regions, a slightly smaller wall thickness (i.e., a reduced cross-sectional area compared to the angle-ply tubes), and variations in the surface finishing of the outer tube surfaces.

Nevertheless, the improved thermal stability of the cross-ply tubes is primarily attributed to their stacking sequence, as the crushing mechanism and overall structural stability of composite tubes are largely governed by the fiber orientations with respect to the tube axis [16]. In cross-ply tubes, the 0° and 90° plies are aligned with the axial and hoop directions, respectively. Under axial impact loading, the 0° plies effectively carry the majority of the load, while the 90° plies provide hoop confinement and stabilize the 0° plies under compressive stresses, thereby preventing premature buckling. These fibers remain structurally active even after moisture uptake or thermal softening, thus preserving the axial load-bearing capacity of the tubes.

The inferior impact performance of the angle-ply tube following hygrothermal and thermal conditioning can be attributed to its greater dependence on matrix-dominated shear transfer and interlaminar integrity, both of which are significantly compromised by moisture absorption and elevated temperatures, as the matrix material becomes weakened under such conditions.

To investigate the permanence of the adverse effects of hygrothermal conditions on the mechanical properties of CFRP tubes, tubes with angle-ply stacking sequences, previously aged by immersion at 75°C, were dried at 40°C for three days. Subsequently, the dried tubes were subjected to axial impact testing. Since hygrothermal exposure had an insignificant effect on the impact response of the cross-ply tube, it was not included in the drying and re-testing procedure. Figure 6 compares the force-displacement responses of the re-dried sample (APRD) with those of both the unaged and hygrothermally aged angle-ply tube (APHG75). The results demonstrate that the adverse effects of hygrothermal aging on the impact response persist even after the redrying process.
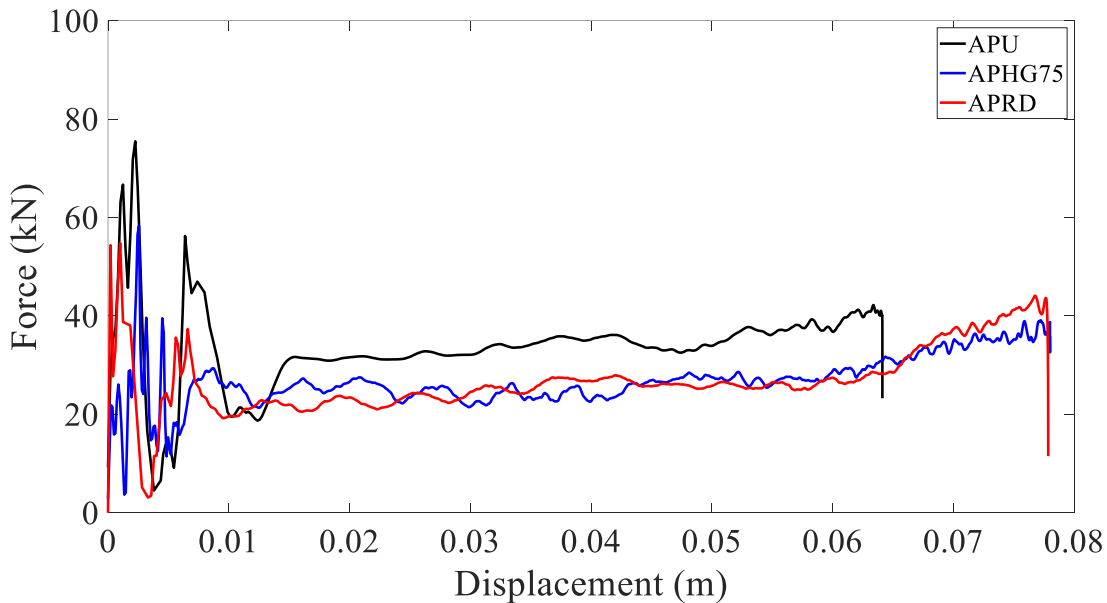
Fig. 6. Force-displacement curves of the unaged, hygrothermally aged (APHG75), and re-dried (APRD) angle-ply CFRP tubes under axial impact loading, illustrating the persistence of hygrothermal degradation effects after redrying.

**3.2.2 Failure Modes and Post-Impact Morphologies**

Both angle-ply and cross-ply tubes exhibited stable progressive crushing under various conditions, including hygrothermal aging, elevated temperature, and unaged states. Figure 7 presents a sequence of images illustrating the crushing process of angle-ply tubes subjected to these different conditions. Splitting aligned with the fiber orientations, along with pronounced interlaminar and intralaminar delamination, is evident in the angle-ply tubes under all three conditions shown in Figure 7. A notable difference between the unaged and the thermally or hygrothermally aged samples is the relatively greater degree of fragmentation observed in the unaged angle-ply tube. This behavior can be attributed to matrix softening induced by thermal and hygrothermal exposure, which increases the ductility of the CFRP material. Furthermore, the unaged angle-ply tube appears to exhibit more extensive separation and the formation of thinner stripes compared to the aged counterparts.
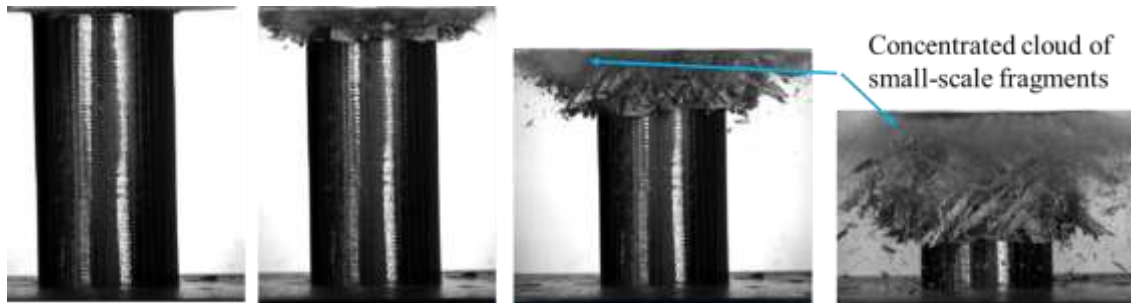
(a)
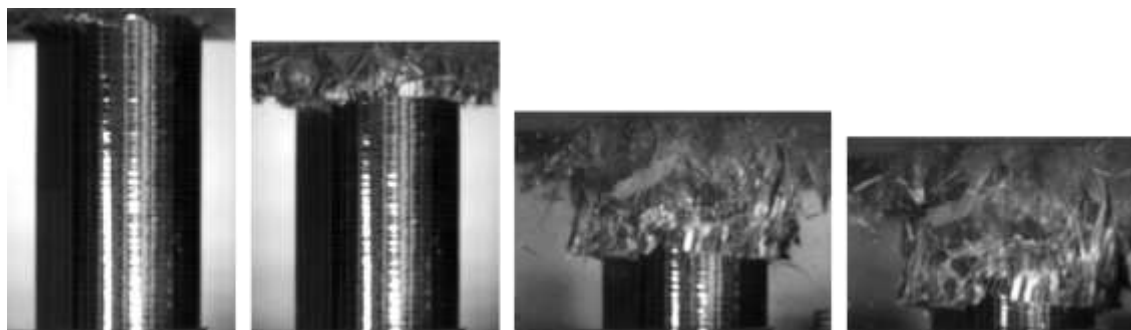
(b)
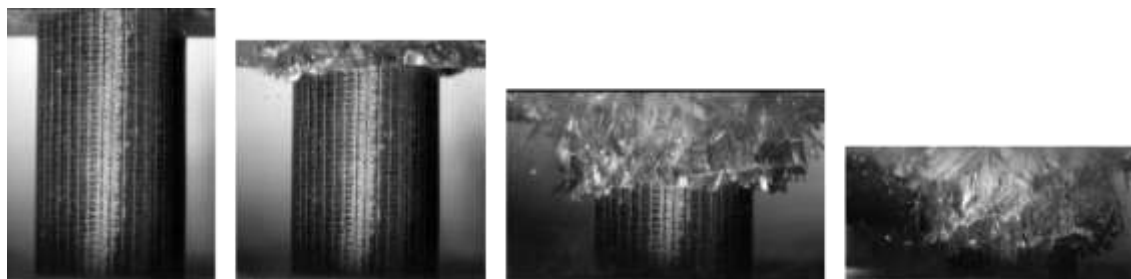
(c)

Fig. 7. Image sequence of the crushing process of angle-ply tubes under different conditions: (a) Unaged tube, (b) Tube at elevated temperature, and (c) Hygrothermally aged tube.

The cross-ply specimens, under various aging conditions, predominantly failed through a brittle fracture mode, characterized by a combination of splaying and fragmentation, as illustrated in Fig. 8. Although the angle-ply specimens exhibited only minor visual differences in crushing behavior across conditions, such variations were even less discernible in the cross-ply specimens. This observation may be attributed to the failure mechanism in cross-ply laminates being more fiber-dominated, whereas in angle-ply laminates, matrix-dominated failure modes are more prevalent.
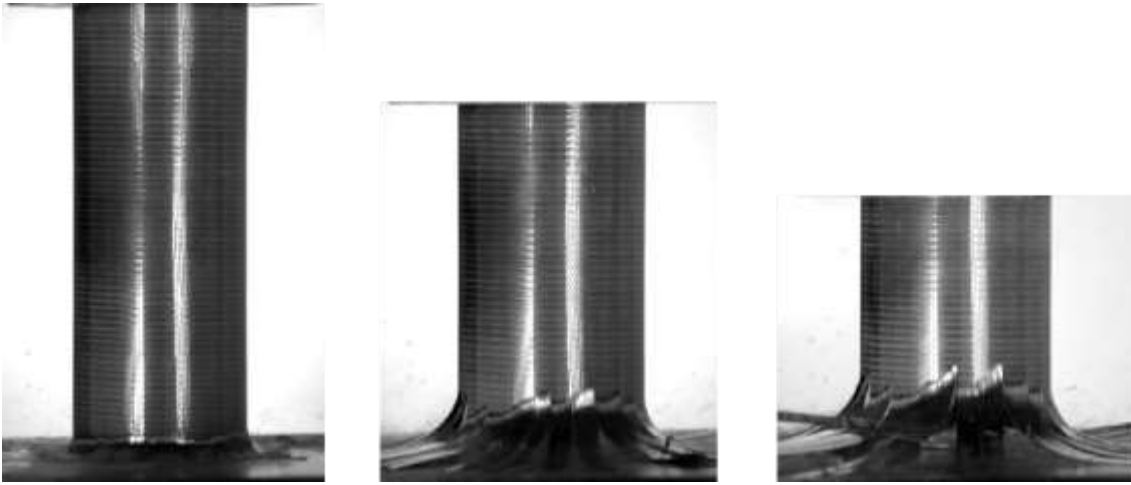
(a)
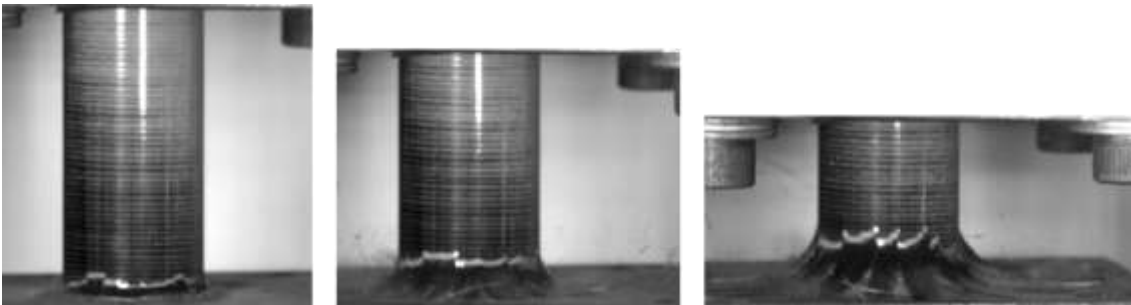
(b)
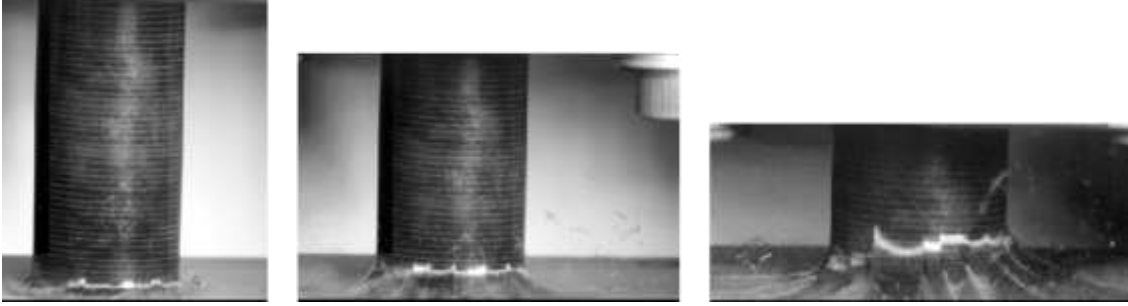
(c)

Fig. 8. Image sequence of the crushing process of cross-ply tubes under different conditions: (a) Unaged tube, (b) Tueb at elevated temperature, and (c) Hygrothermally aged tube.

Figure 9 presents the top view of the impacted samples subjected to various aging conditions. For both cross-ply and angle-ply tubes, distinguishing the testing condition based solely on the macroscopic damage morphology is challenging. This indicates that the softening effects induced by thermal and hygrothermal aging did not result in notable alterations to the observable damage patterns. Instead, these environmental conditions primarily induced microscopic changes, particularly the softening of the epoxy matrix, which adversely affected the impact performance of the aged tubes. However, these effects did not lead to significant changes in the overall crushing modes when compared to the unaged specimens.

The angle-ply stacking sequence incorporates ±45° plies primarily oriented to provide shear and torsional strength. Under axial impact loading, these plies contribute less directly to axial load-bearing compared to 0° plies. However, they play a critical role in stabilizing the crushing process through interlaminar shear resistance. When subjected to thermal or hygrothermal exposure, such as elevated temperature or moisture absorption, the matrix may undergo plasticization, microcracking, or fiber–matrix interfacial debonding. These degradations reduce the shear stiffness of the ±45° plies, compromising their stabilizing function and leading to premature delamination and impairing the axial impact performance. Consequently, hygrothermal aging weakens the fiber–matrix bond, promotes early onset of failure, and reduces energy absorption capacity. In contrast, cross-ply laminates rely more on the 0° fibers aligned with the loading direction for axial load-bearing. The fibers aligned in the hoop direction (90°), however, provide high hoop resistance and make the 0° fibers more stable under compressive load. So the mechanical properties in both axial and hoop directions are governed by fibers, as a result, their

structural integrity is less sensitive to moderate matrix degradation, with failure typically governed by fiber fracture and global crushing rather than matrix-dominant failure modes. Thus, although it is reported in Ref. [16] that SEA values for both cross-ply and angle-ply in room temperature (unaged condition) are equal, the angle-ply tube exhibits greater sensitivity to environmental degradation in terms of energy dissipation performance.
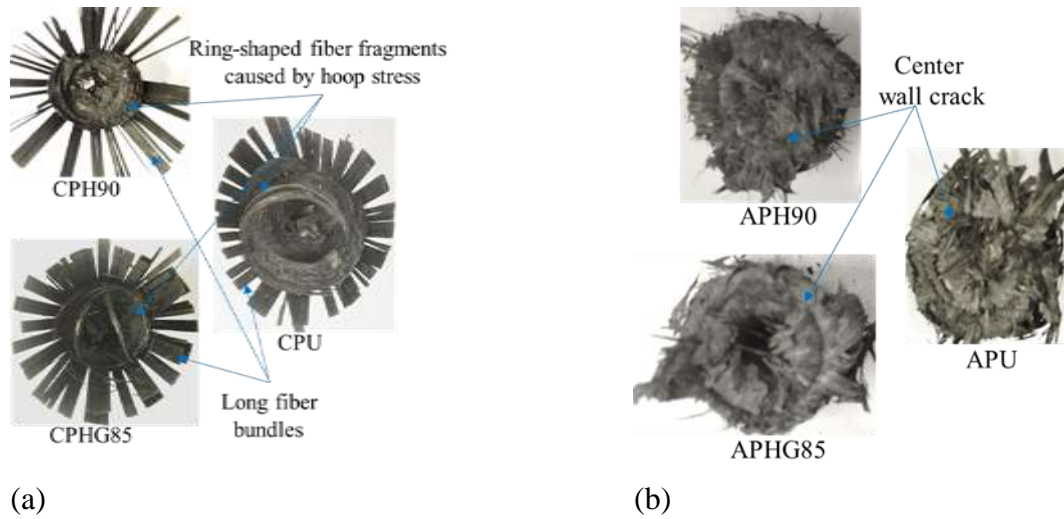

(a)   (b)

Fig. 9. Top view of impacted cross-ply and angle-ply tubes under different aging conditions; (a) Cross-ply samples (CPU: cross-ply unaged; CPH75: cross-ply aged at an elevated temperature of 75 °C; CPHG75: cross-ply subjected to hygrothermal aging at 75 °C), and (b) Angle-ply samples (APU: angle-ply unaged; APH75: angle-ply aged at an elevated temperature of 75 °C; APHG75: angle-ply subjected to hygrothermal aging at 75 °C.)

4. Conclusions

The effect of short-term hygrothermal and thermal conditions on the axial impact performance of CFRP tubes with different stacking sequences, including cross-ply and angle-ply lay-ups, is investigated experimentally. Some tubes were exposed to elevated temperatures below the glass transition temperature (Tg) of the resin, specifically at 50 °C and 75 °C, while others were aged by submersion in distilled water at room temperature and at 75 °C. Both thermal and hygrothermal exposures negatively affect the crashworthiness of the CFRP tubes by softening (i.e., weakening) the epoxy matrix. However, exposure to elevated temperature alone induces a more pronounced degradation in the load-bearing capacity of the tubes compared to hygrothermal aging.

It was observed that the stacking sequence influences the moisture absorption capacity of CFRP tubes under accelerated hygrothermal conditions, specifically when immersed in water at elevated temperatures. The angle-ply configuration ([±45/0…]) exhibited approximately twice the moisture uptake compared to the cross-ply configuration ([0/90…]). The detrimental effect of hygrothermal aging on the impact performance of both tubes correlated with their respective levels of moisture absorption. Hygrothermal exposure at room temperature resulted in the lowest moisture uptake and had a relatively negligible impact on the specific energy absorption (SEA) values when compared to the unaged specimens.

In addition to their superior resistance to moisture absorption, the cross-ply tubes demonstrated greater thermal stability and enhanced crushing performance at elevated temperatures compared to the angle-ply specimens. This behavior can primarily be attributed to the fiber-dominated crushing and energy absorption mechanism in cross-ply tubes, given that carbon fibers are significantly less sensitive to elevated temperatures than the epoxy matrix. In contrast, the crushing response of angle-ply tubes is more matrix-dominated, making them more susceptible to degradation under elevated temperature and hygrothermal conditions, which in turn leads to a more pronounced reduction in their energy absorption capabilities.

In the present study, short-term aging conditions were applied to CFRP tubes at temperatures below the glass transition temperature (T_g) of the epoxy resin. It is expected that higher temperatures and longer exposure durations would result in more pronounced effects on the mechanical performance of the tubes. Furthermore, aging under real environmental conditions, where various mechanical stresses are simultaneously imposed on the composite components, may intensify the degradation caused by thermal and hygrothermal factors, leading to further deterioration in mechanical properties.

Material Characterization of HX700 and ZSTE 380 and Crash Box Design Tests for Marcopolo

The scope of this project encompasses the following activities:

1. **Material Characterization for Johnson–Cook Plasticity Model Development**
   - Execution of mechanical tests at various strain rates to calibrate the Johnson-Cook constitutive model parameters for steel materials.
   - Testing campaigns include:
     - **Quasi-static tensile tests** to determine baseline mechanical properties.
     - **Low and intermediate strain rate tests** utilizing an impact tensile test device.
     - **High strain rate tests** were conducted with a Split Hopkinson Tensile Bar (SHTB) apparatus.

2. **Quasi-static and Axial Impact Testing of Steel Tubes with Different Trigger Mechanisms**
   - Design and execution of quasi-static compression tests on steel crash tubes with various energy-absorbing trigger mechanisms (e.g., chamfered, corrugated, or other geometries).
   - Drop-weight impact tests to evaluate the dynamic crushing behavior and energy absorption performance under realistic crash conditions.

Conducting 15 axial impact tests and 10 quasi-static compression tests on ZSTE tubes.

3. **Development of Numerical Models**
   - Construction and calibration of finite element models to simulate the quasi-static and dynamic response of the characterized materials and crash boxes.
   - Implementation of the Johnson-Cook plasticity model into numerical simulations.
   - Validation of the numerical models against experimental data from mechanical and impact tests.

The impact tests were used to calibrate the JC plasticity model parameters found for ZSTE material.
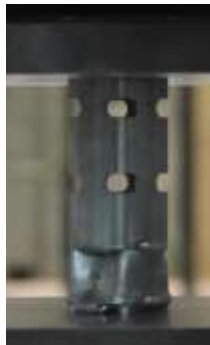
| Trigger 1 | Trigger 2 (bigger tube) | No Trigger |

Examples of axial impact tests on tubes having different trigger
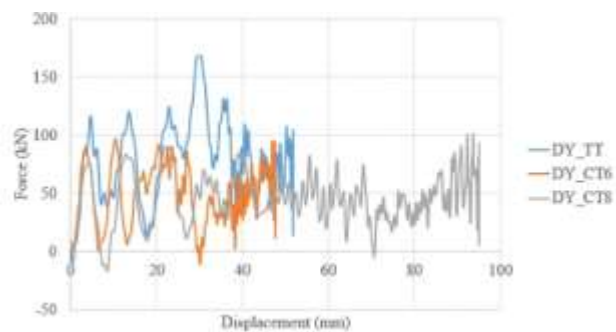

| Trigger 1 | Trigger 2 (bigger tube) | No Trigger |

Examples of axail quasi-static compression tests on the tubes having different trigger
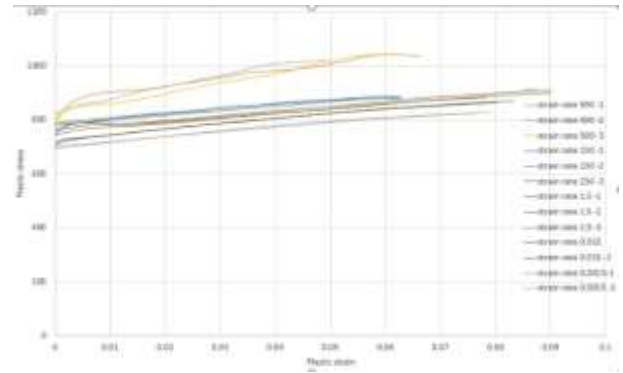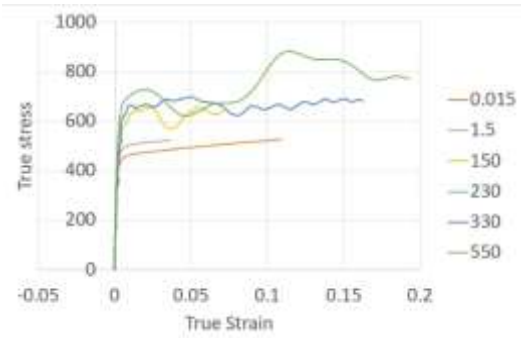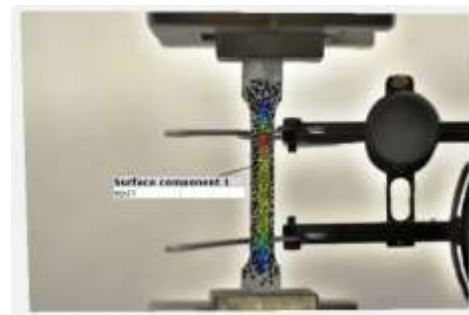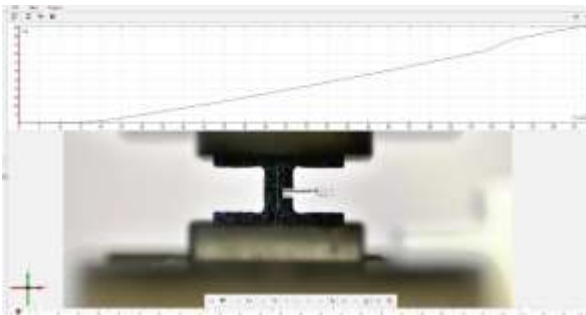

Force-displacement of quasi-static   Force-displacement of impact tests

Examples of force displacement, are calculated from high-speed image processing using GOM software.

ZSTE material (stress-strain curves at different strain rates)

Plastic stress-strain curves of HX material

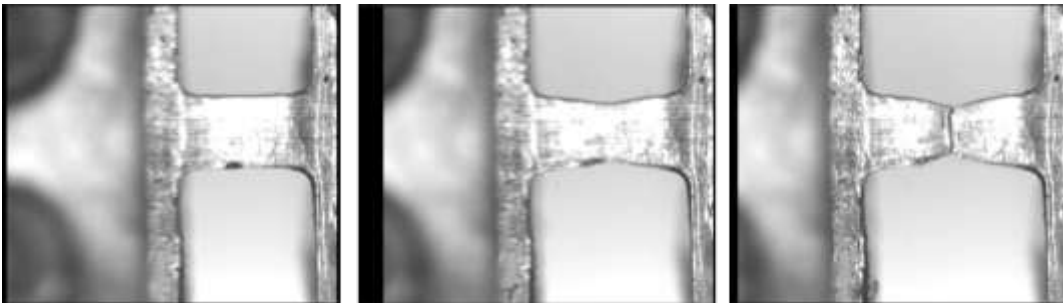Tensile strain for all tests is measured using DIC (virtual extensometer)

Image sequence of SHTB tests on ZSTE material

Average values for JC parameters for HX material (reference strain rate = 0.015)

A	B	n	c
695	1104	0.8234	0.0126

Average values for JC parameter for ZSTE (reference strain rate = 0.015)

A	B	n	C
436.917	230.635	0.430	0.027